PREDICTING HIGH-SPEED MILLING DYNAMICS USING STEREOLITHOGRAPHY

A Dissertation by

Akale Merid Tola

Master of Science, Wichita State University, 2002

Bachelor of Science, Addis Ababa University, 1984

Submitted to the Department of Industrial and Manufacturing Engineering
and the faculty of Graduate School of
Wichita State University
in partial fulfillment of
the requirements for the degree of
Doctor of Philosophy

December 2010

PREDICTING HIGH-SPEED MILLING DYNAMICS USING STEREOLITHOGRAPHY

The following faculty members have examined the final copy of this dissertation for form and content, and recommend that it be accepted in partial fulfillment of the requirement for the degree of Doctor of Philosophy with a major in Industrial Engineering.

_____
Gamal S. Weheba, Committee Chair

_____
Krishna Krishnan, Committee Member

_____
Mehmet B. Yildirim, Committee Member

_____
Hamid M. Lankarani, Committee Member

_____
Michael McCoy, Committee Member

Accepted for the College of Engineering

_____
Zulma Toro-Ramos, Dean

Accepted for the Graduate School

_____
J. David McDonald, Dean

DEDICATION

To my wife Tsigie for her unending encouragement;
my son Noah and my daughter Destinee, who have sacrificed their time in support of this effort;
my brother Sileshi and my friends, who gave me the courage to finish this dissertation

ACKNOWLEGEMENTS

I would like to thank my dissertation committee chair, Dr. Gamal Weheba, for his professional advice, suggestions, mentoring, encouragement, and patience throughout my academic study and research. Without him, completion of this dissertation would not have been possible.

I would also like to extend my gratitude to members of my committee, Dr. Krishna Krishnan, Dr. Mehmet B. Yildirim, Dr. Hamid M. Lankarani, and Dr. Michael McCoy, for their helpful comments and suggestions on this dissertation.

Special thanks go to Dr. Michael McCoy for his invaluable help in advising and mentoring me through this critical part of my studies.

Thanks to all my friends who provided me assistance during laboratory testing.

Finally, I express my heartfelt appreciation to Tsigie, my wife, who has provided me with her love, support, and understanding. She is always my inspiration, and I would never have been able to accomplish my education without her.

ABSTRACT

Stereolithographic (SL) models have been successfully utilized during product development and the early stages of process design. In this research, SL models were utilized to predict the natural frequencies of high-speed cutting tools. Most common practices utilize theoretical or numerical methods to evaluate tool designs by using simplifying assumptions. However, these results may fail to accurately predict stability limits of the machining system.

This research developed a proactive approach for evaluating tool design, which minimizes the risk of ordering the wrong tool and sacrificing the most economic machining condition. Experiments have indicated that SL models correlate well with test results performed on actual machining systems. Consequently, SL models of selected tool designs were constructed and utilized to predict the dynamic characteristics and the stability limits of the machining system.

Using stereolithographic models, practitioners can generate stability lobe diagrams and study tool design alternatives before producing or ordering a required tool.

TABLE OF CONTENTS

TABLE OF CONTENTS (continued)

LIST OF TABLES

LIST OF TABLES (continued)

Table Page

LIST OF FIGURES

LIST OF FIGURES (continued)

Figure Page

LIST OF ABREVIATIONS

ANOVA	Analysis of Variance
BC	Boundary Condition
CAD	Computer-Aided Design
COV	Coefficient of Variation
CT	Carbide Tool
3DP	Three-Dimensional Printing
EMA	Experimental Modal Analysis
FDM	Fused Deposition Modeling
FE	Finite Element
FEM	Finite Element Method
FFBC	Free-Free Boundary Condition
FRF	Frequency Response Function
HSM	High-Speed Machining
Im(G)	Imaginary-Part Frequency Response Function
LOM	Laminated Object Manufacturing
MRR	Material Removal Rate
OH	Overhang
Re(G)	Real Part Frequency Response Function
RP	Rapid Prototyping
SDOF	Single Degree of Freedom
SL	Stereolithography
SLA	Stereolithography Apparatus

SLD	Stability Lobe Diagram
SLS	Selective Laser Sintering
UV	Ultraviolet

LIST OF SYMBOLS

v	cutting speed, peripheral velocity of cutter (mm/s)
N	spindle peed (rpm)
d	diameter (mm)
T	instantaneous torque (Nm)
F_t	tangential force
z	number of teeth in cutter
P	power (watt)
a	depth of cut (mm)
h	chip thickness (mm)
s_z	feed per teeth (mm/tooth)
s	feed rate (mm/sec)
τ	time delay (sec)
f_t	tooth pass frequency (Hz)
k_s	cutting specific power
x	displacement of the cutter normal to cut
t	time
m	mass
c	damping coefficient
k	stiffness (N/m)
r_t	ratio of f_c / f_n
f_1	minimum peak frequency
f_2	maximum peak frequency

f_c	chatter frequency
f_n	natural frequency
ζ	ratio of damping coefficient c to critical damping coefficient c_c where critical damping coefficient $c_c = 2\sqrt{km}.$
z^*	average number of teeth in cut
σ	standard deviation

CHAPTER 1

INTRODUCTION

The key to successful business is always dependent on quality, productivity, and cost. High-speed machining (HSM) is commonly defined as a strategy for achieving high productivity and increased material removal rate (MRR) through a spindle speed exceeding 10,000 rpm, and cutting speed exceeding 914 ft/min (279 m/min) for nonferrous applications or exceeding 305 ft/min (93 m/min) for steel and cast iron applications.

Erdel (2003) indicated that HSM allows manufacturing companies to respond quickly to sudden market shifts and different product mixes. Shaw (2005) pointed out that high-speed milling is a widely used HSM process for producing flat and curved surfaces using multipoint cutting tools. Dalton et al. (2008) indicated that the profitability of a high-speed milling process is highly dependent upon the stability of the dynamics of the machining system, which in turn limits the value of the cutting parameters, such as spindle speed and the axial cutting depth that may be selected. They indicated that employing an HSM strategy leads to the primary concern of chatter, a self-excited vibration between the cutting tool and the workpiece.

The history of chatter investigation in machining has been rich. The first evidence and description of chatter was made by Taylor (1907) who stated that chatter is the ~~"m~~most obscure and delicate of all problems facing the machinist." Since then, many researchers have investigated chatter and ways to prevent it through modeling of machining system dynamics. Some applications of orthogonal chatter theory remain to be implemented, due to complications involved in cutting forces and chip-flow directions in milling operations (Altintas, 2000). This includes the contribution of intermittent cutting periods towards the underlying assumptions that neglect cutting-tool geometry.

The advancement of technology and application of stereolithography (SL) have shown the successful utilization of SL models during product development and early process design stages. This research mainly focused on using SL models to predict the dynamic characteristics of cutting tools in the spindle-tool machining system. This research was aimed at overcoming the core limitations in the traditional models. Dynamic characteristics of SL models were investigated and compared with those of actual cutting tools. Scaling factors that can correlate the results of testing SL models to those obtained from testing actual tools were calculated. Eventually, these scaling factors were used to develop a procedure for predicting the stability limits of the machining system.

This dissertation contains seven chapters. While this chapter offered a brief introduction, Chapter 2 presents a review of the literature pertaining to chatter generation in high-speed machining, rapid prototyping and its applications for dynamic testing. A discussion of cited work towards identifying research gaps is provided in Chapter 3. Chapter 4 presents the research objectives and outlines the procedure followed. An initial investigation of the usefulness of SL models in predicting the dynamic characteristics of carbide barstock is also represented. In Chapter 5, the effects of changes in boundary conditions and tool geometry on the predicted dynamic characteristics are quantified. The results were used to establish appropriate conditions for testing actual carbide tools and their respective SL models on a given machining system. Results of these tests were used to calculate scaling factors required to predict the dynamic characteristics of the machining system and determine its stability limits. Chapter 6 represents a verification of the research procedure and illustrates its accuracy in evaluating proposed tool designs. Final conclusions and recommendations for future research are provided in Chapter 7.

CHAPTER 2

LITERATURE REVIEW

This chapter presents a review of chatter in high-speed machining and its prevention, as well as rapid prototyping and its application for dynamic testing. The literature review is divided into two sections. The first section deals with chatter generation in high-speed machining, which includes the definition and physical characteristics of chatter, chatter-prevention models, generation of stability lobe diagrams (SLDs) for prevention of chatter, and methods used to validate the models. The second section includes the rapid prototyping that particularly deals with stereolithography and applications for dynamic testing.

2.1 Chatter Generation in High-Speed Machining

The investigation of chatter generation and machining, particularly milling stability has a rich history. The work by Arnold (1946) considered the negative damping effect as the source of chatter. Chatter prevention models that include early detection and control for turning processes were suggested by Tlusty (1965). This resulted in the creation of the well-known stability lobe diagrams. These models were considered to handle a system with a single degree of freedom (SDOF), a unidirectional system with two degrees of freedom, and a system with two degrees of freedom in different directions. Tlusty (1986) modified his turning analysis to accommodate the milling process. SLDs create boundaries that identify stable and unstable cutting regions separated by lobes of stability as a function of the axial depth of cut and machine spindle speed.

2.1.1 Definitions and Physical Characteristics

Prior to defining chatter, it is necessary to identify four other important terms related to high-speed milling performance (Schmitz and Smith, 2008): cutting speed, torque, spindle power, and material removal rate.

a. The cutting speed, ν, or the peripheral velocity of the cutter, is described as

$$\nu = \frac{2\pi rN}{60} = \frac{\pi dN}{60}(mm/s) \tag{1}$$

where N is given in rpm, and the tool radius r (or diameter d) is given in mm. This quantity is important because cutting temperature increases with cutting speed. High temperature at the tool-chip interface can lead to tool wear and limit the cutting speed, and may also reduce the availability of large stable zones in high-speed milling.

b. The machine spindle must possess the required torque to continue rotating the tool against the retarding tangential component of the cutting force for any cut to be performed. The instantaneous torque, T, is expressed as the sum of the product of the tool radius r and the tangential force F_t for each tooth engaged in the cut. Torque can be written as

$$T = \sum_{j=1}^{z} r.F_{t,j} = r\sum_{j=1}^{z} F_{t,j} \tag{2}$$

where z ($z = 1,2,..j$) is the number of teeth in the cutter, and the typical unit for T is Nm. For most spindles, the available torque is spindle-speed dependent and provided as a ~~–t~~orque curve" with spindle specifications.

c. Similar to torque, the available spindle power can limit the potential cutting geometry (i.e., if the power is exceeded, the spindle will stall). Power is determined from the product of torque T and rotational speed N. If the spindle speed is expressed in *rpm* and the torque is *N-m*, then the power P is

$$P = \frac{TN.2\pi}{60} \tag{3}$$

Spindle power is a function of spindle speed and expressed via the "power curve" supplied by the specific spindle manufacturer.

d. In order to reduce machining time, and subsequently cost, it is desired to increase the material removal rate or volume of material per unit of time:

$$MRR = ahs = ahs_z zN \tag{4}$$

where a is depth of cut, h is chip thickness, s_z is feed per teeth, and s is the feed rate.

Tobias (1965) defined that chatter is a form of self-excited vibration may be caused by regeneration of chip thickness or mode coupling. Regenerative chatter results from phase differences and explained by a wavy surface finish left during the previous tooth in milling is then removed during the succeeding revolution or tooth period and also leaves a wavy surface due to structural vibration. Mode Coupling occurs later than regenerative chatter when there are vibrations in two directions in the plane of cut.

According to Smith (1990), chatter is such a vibration due to the interaction of the dynamics of the chip removal process together with the structural dynamics of the machine tool. This type of chatter tends to be at very high amplitude, which can result in either damage to the machine tool or premature failure. In addition, they pointed out that chatter is initiated by a disturbance in the cutting zone for several reasons:

- Lack of homogeneity (in the workpiece material, i.e., typically a porous component, such as that found in a powder metallurgy compact).
- Workpiece surface condition (i.e., typically a hard oxide scale on a hot-rolled steel component, utilizing a shallow depth of cut).

- Workpiece geometry (i.e., if the component shape produces either a variation in the depth of cut, for example, because of uneven depth of casting material being machined, or light cuts on interrupted shapes, such as hexagon, square, or rectangular bar stock).
- Frictional conditions (i.e., tool/chip interface frictional variations while machining).

The regenerative chatter shows that there is a time-delayed surface-generation step occurrence from tooth-to-tooth in milling (Tlusty, 1986). This occurs in a manner from revolution to revolution in turning operations. The time delay τ is given by

$$\tau = \frac{60}{Nz} \tag{5}$$

and the tooth pass frequency f_t is given by

$$f_t = \frac{1}{\tau} = \frac{N.z}{60} \tag{6}$$

Degarmo et al. (2003) provided a list of factors that can indicate the onset of chatter:

- Sudden onset of vibration, the amplitude of which will rapidly increase until a maximum threshold-saturation, is reached, i.e., sounding like either a screech, whine, or buzz.
- A frequency that is close to that of the machining system's natural frequency, whereby the largest force-displacement response occurs at a resonance that enables the maximum dissipation of energy.
- Unacceptable surface textures with visual appearance, as shown in Figure 1.

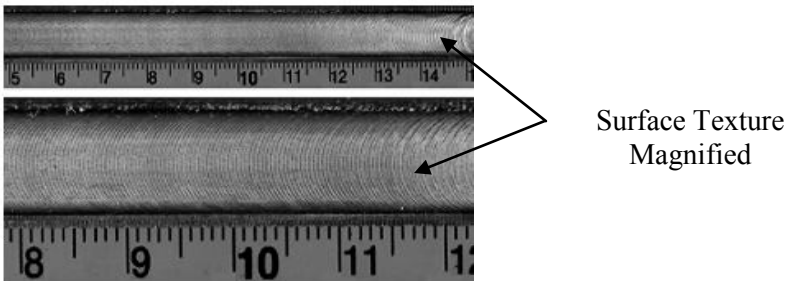

Figure 1. Workpiece showing transition from stable cut to cut with chatter (Faassen, 2007).

Tobias (1965) discussed the occurrence of chip thickness variation with respect to physical characteristics of the onset of chatter, as shown in Figure 2.

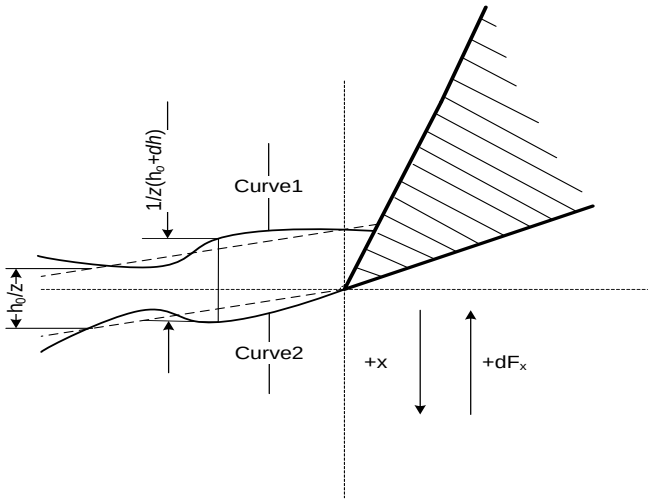

Figure 2. Effect of chip thickness variation in end milling (Tobias, 1965).

The transition of the stable cut to the cut with chatter is also shown in Figure 1, where the wavy surface was left by the previous tooth and the current cutter vibration. For investigation of dynamic stability, Tobias assumed that vibration $x(t)$ is superimposed on the steady-state feed of the tool h_o. Figure 2 shows one of the cutting edges of the tool at time t. Under vibration-free conditions, this edge would remove a constant chip thickness of h_o/z (z = # of cutting edges), as indicated by the dashed line. The surface at which the chip is removed has a wavy rather than flat form, as the result of vibration $x(t)$, indicated by *Curve1*. The surface of the chip was cut at an earlier time t-$\boldsymbol{T}/z$ by the other cutting edge ($\boldsymbol{T} = 1/\boldsymbol{N}$ = time for one revolution of the end mill), and at that time, the vibration x had already occurred. Starting from $t = 0$ onwards, the cutting edge that is in actual contact moves along *Curve2*, and then the instantaneous value of the chip thickness becomes $(h_0+dh)/z$. Hence, the chip thickness variation for end milling is given by

$$\frac{1}{z}dh = x(t) - x(t-\tau) \tag{7}$$

Milling technology has advanced in the last couple of decades, and the importance of modeling and predicting stability has increased immensely, as noted by Budak (2006a). The following sections discuss three important models that were recently developed and implemented for chatter prevention.

2.1.2 Chatter Prevention Models

Chatter-prevention models have recently been suggested, developed, and utilized through the creation of stability lobe diagrams for high-speed milling processes. These models are usually based on either frequency domain or time domain. The modified model by Tlusty (1986) used an average tooth-angle approach and solved the problem for time dependence of the cutting force direction. Altintas and Budak (1995, 1998) provided an analytical chatter-prediction model, which considered milling cutters that had two-orthogonal degrees of freedom. They used a Fourier series approach for creation of an SLD that was dependent on the radial immersion and yet still similar to Tlusty's approach in estimating the average cutting force.

In orthogonal cutting, the cutting force F is proportional to the cutting area, i.e., the product of the chip width or depth of cut a, and thickness h, from Merrit (1965):

$$F = k_s a \Delta h = k_s a\{x(t) - x(t-\tau)\} \tag{8}$$

where k_s is the cutting specific power, x is the displacement of the cutter normal to the cut, t is the time, and τ is the time delay between two teeth cuts.

In order to provide the basic physical insight into the dynamic behavior of the machining dynamics, it is important to analyze a single-degree-of-freedom system. The equation of motion for the SDOF system is

$$m\ddot{x} + c\dot{x} + kx = F \tag{9}$$

Substituting equation (8) into equation (9) yields

$$m\ddot{x} + c\dot{x} + kx = k_s a \Delta h = k_s a\{x(t) - x(t-\tau)\} \tag{10}$$

The derived equation from equation (10) is given by

$$\begin{aligned} \frac{X}{F} &= \frac{1-r^2}{k\left((1-r^2)^2 + (2\xi r)^2\right)} + i\frac{-2\xi r}{k\left((1-r^2)^2 + (2\xi r)^2\right)} \\ &= \mathrm{Re}[G_{orient}] + i\,\mathrm{Im}[G_{orient}] = G \end{aligned} \tag{11}$$

where m = mass, c = damping coefficient, k = stiffness ($k = F / x$), r = ratio of chatter frequency f_c to natural frequency (f_n), and ζ = ratio of damping coefficient c to critical damping coefficient c_c, where the critical damping coefficient $c_c = 2\sqrt{km}$.

2.1.3 Generating Stability Lobe Diagram for Chatter Prevention

A plot that distinguishes between the stable and unstable boundaries of the axial depth of cut with respect to the spindle speed of a machine is called a stability lobe diagram. The occurrences of stable cuts are limited to the region below the stability boundary line, while unstable cuts are found within the region above the stability boundary line. A theoretical SLD indicating these stable and unstable regions is shown in Figure 3. The required chatter-free axial cutting depth can be obtained by increasing the spindle speed rather than slowing it down as in the traditional method. For example, as shown in Figure 3, a_1, the initial axial depth of cut at spindle speed N_1, can be increased to depth of cut a_2 at an increased spindle speed N_2, rather than slowing it down to N_0, a_0, or somewhere in the middle between N_0 and N_1.

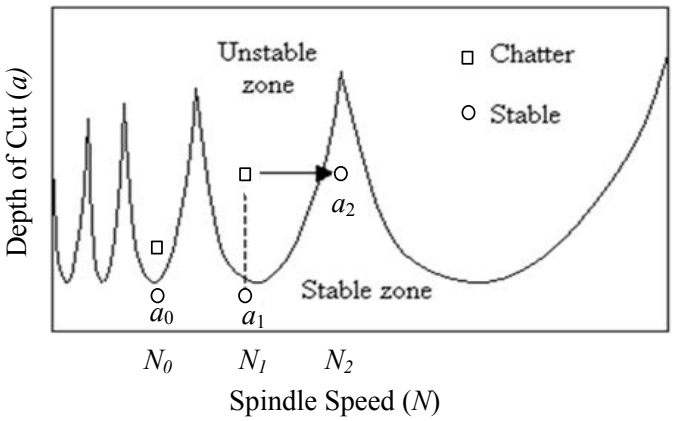

Figure 3. Example of stability lobe diagram (Schmitz and Smith, 2008).

Two approaches are used to create a stability lobe diagram, namely, the average tooth-angle method and the Fourier series approach. Tlusty et al. (1983) assumed an average tooth angle in the cut to address the cutting-force direction time-dependence and then considered an average force direction. This created an autonomous or time invariant system. They then made use of directional orientation factors to, first, project the force into *x* and *y* mode directions and, second, project these results onto the surface normal. Depending on the feedback system or gain, represented by chip width or depth of cut *a,* and the spindle speed *N,* the milling operation is either stable or exhibits chatter. The modified form of equation for stability limit is given by

$$a_{\min} = \frac{-1}{2k_s \,\mathrm{Re}[G_{orient}]z*} \tag{12}$$

where k_s is the cutting stiffness of the work piece or specific power, $z*$ is the average number of teeth in the cut (i.e., the extent of radial immersion), and $\mathrm{Re}(G_{orient})$ is the oriented frequency response function (FRF) of the real part. The terms G_{orient} or FRF_{orient}, the oriented frequency response functions of the real or imaginary parts, respectively, are calculated by summing the products of the directional orientation factors and corresponding FRFs or Gs for the *x* and *y* directions:

$$G_{orient} = FRF_{orient} = \mu_x G_x + \mu_y G_y \tag{13}$$

where, for example in the slotting operation case in Figure 4, $\mu_x = \cos(\beta)\cos(0)$ and $\mu_y = \sin(\beta)*\cos(90)$, and β is the cutting force angle. The Re(G)s for the x and y directions are obtained from the test results, as shown in Figure 5(a) (magnitude response) and 5(b) (real part of FRF).

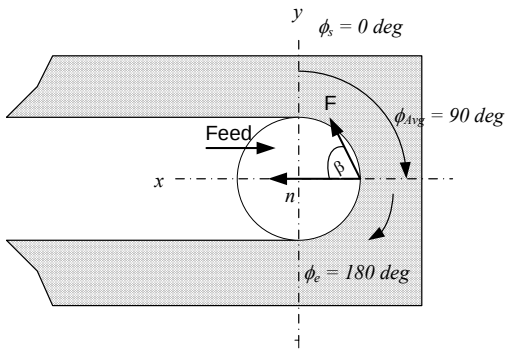

Figure 4. Geometry for determining slotting directional orientation factors (Schmitz and Smith, 2008).

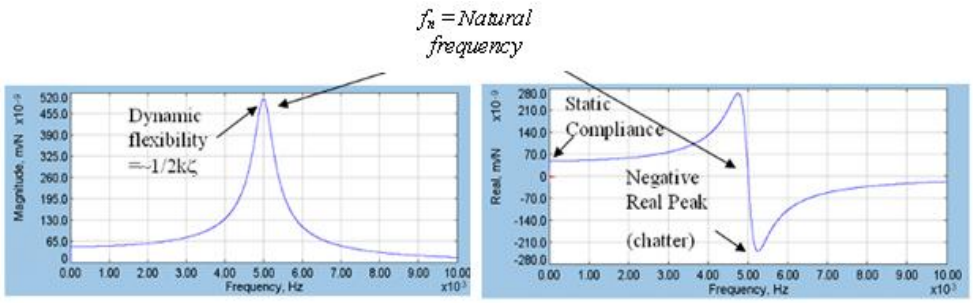

(a) (b)

Figure 5. Frequency response function: (a) magnitude response and (b) real part (Manufacturing Laboratories, Inc., http.//www.mfg-labs.com/, 4/17/2009).

The average number of teeth in the cut z^* during the milling process is calculated as

$$z^* = \frac{z(\phi_e - \phi_s)}{360} \tag{14}$$

where ϕ_s and ϕ_e are the immersion angles at start and end, respectively.

According to the regenerative chatter theory given by Tlusty (1986), chatter occurs whenever there is a shift in the phase angle ε between the current and previous surface waviness. Therefore, the ratio of chatter frequency f_c to tooth-pass frequency f_t represents the number of surface waves between consecutive cutter teeth and can be written as an integer *j,* also known as the lobe number, where *j = 0, 1, 2…* plus a fraction of $\varepsilon/2\pi$ radians:

$$r_t = \frac{f_c}{f_t} = j + \frac{\varepsilon}{2\pi} \tag{15}$$

where r_t is the ratio between the tooth-pass frequency f_t and natural frequency f_n. The phase shift angle ε is expressed by Tlusty (1986) as

$$\varepsilon = 2\pi - 2\tan^{-1}\left(\frac{\mathrm{Re}[G_{orient}]}{\mathrm{Im}[G_{orient}]}\right) \tag{16}$$

where the real and imaginary $\mathrm{Re}[G_{orient}]$ and $\mathrm{Im}[G_{orient}]$ are both negative from equation (11). Using the principal range of $-\pi/2 < \tan^{-1} x < \pi/2$ yields $0 < \tan^{-1}\left(\frac{\mathrm{Re}[G_{orient}]}{\mathrm{Im}[G_{orient}]}\right) < \pi/2$, and the phase shift angle ε is between π and 2π, or $\pi < \varepsilon < 2\pi$. Substituting equation (11) into equation (16), and then into equation (15) gives the regenerative chatter equation:

$$\frac{f_c}{f_t} = \frac{r_c}{r_t} = j + 1 - \frac{1}{\pi}\tan^{-1}\frac{1-r_c^2}{2\xi r_c} \tag{17}$$

By substituting equation (6) into equation (17), the relationship between the spindle speed *N* (*rpm*) and the chatter frequency f_c is obtained as

$$N = \frac{60 f_c}{z}\left(j + 1 - \frac{1}{\pi}\tan^{-1}\frac{1-r_c^2}{2\xi r_c}\right)^{-1} \tag{18}$$

Tlusty's procedure for generating milling SLDs is as follows:

a. Determine the oriented G, and identify the valid chatter frequency range(s), i.e., where the real part is negative.
b. Solve for ε, the phase between the current and previous tooth vibrations over the valid frequency range(s).
c. Find the average number of teeth in the cut for the selected radial immersion.
d. Calculate $a_{\min}$ over the valid frequency range(s).
e. Select a j value (integer number of waves between teeth), and calculate the associated spindle speeds over the valid frequency range(s).
f. Plot the spindle speed N versus depth of cut $a_{\min}$ (both a function of the same frequency vector, so that the first spindle-speed value corresponds to the first limiting-chip width or depth of cut, and so on) for each j value (j = 0, 1, 2,…).

Therefore, any $(N, a_{\min})$ pair that appears above the collective boundary indicates unstable behavior, while any pair below the boundary indicates stable cutting.

Altintas and Budak (1995, 1998) used an alternative technique to transform the dynamic milling equations into a time-invariant, but radial-immersion-dependent system. Similar to Tlusty, they approximated the time-dependent cutting forces by an average value but employed a different approach to identify the mean. Instead of using the average angle of the tooth in the cut, they preferred to use the time-varying coefficients of the dynamic milling equations that depend on the angular orientation of the tool as it rotates through the cut, expand it into a Fourier series, and then truncate the series to include only the average component. They indicated that the structural excitation of cutting forces in the feed and normal directions would cause dynamic displacements in the x and y directions, respectively. The cutting force excites the structure causing deflections in the two perpendicular directions in the plane of the cut. These deflections

are carried to the rotating tooth number (j) in the radial or chip thickness direction by its projection onto v_j, where $v_j = -x\sin(\phi_j) - y\cos(\phi_j)$, and ϕ_j is the instantaneous angular immersion of tooth j, as shown in Figure 6.

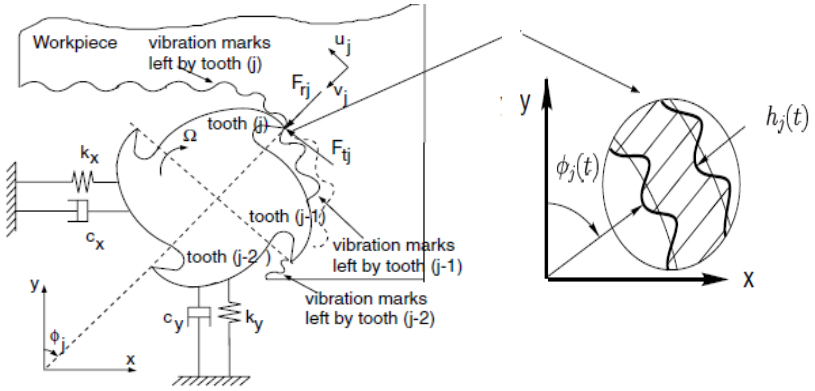

Figure 6. Mechanism of chatter in milling process (Altintas, 2000).

The revised expression to create a stability limit for a chatter-free axial depth of cut $\widetilde{a}_{\lim}$ is

$$\widetilde{a}_{\lim} = \frac{2\pi}{zk_t(\lambda_{\mathrm{Re}}^2 + \lambda_{\mathrm{Im}}^2)}\lambda_{\mathrm{Re}}(1+\widetilde{\kappa}^2) \tag{19}$$

where k_t is the cutting force factor, λ_{Re} and λ_{Im} are the real and imaginary parts of the transfer function, respectively, and $\widetilde{\kappa} = \dfrac{\lambda_{\mathrm{Im}}}{\lambda_{\mathrm{Re}}}$. The corresponding phase angle is

$$\widetilde{\varepsilon} = \pi - 2\tan^{-}(\frac{\lambda_{\mathrm{Im}}}{\lambda_{\mathrm{Re}}}) \tag{20}$$

$$\widetilde{\tau} = \frac{1}{\omega_c}(\widetilde{\varepsilon} + j2\pi) \tag{21}$$

where $\widetilde{\tau} = \dfrac{60}{z\widetilde{N}} = \dfrac{1}{f_t}$ is the corresponding tooth-passing period, f_t is the tooth-passing frequency, ω_c is the angular chatter frequency, and $\widetilde{N}$ is the modified spindle speed in *rpm*. Substituting equation (20) into equation (21) yields

$$\tilde{N} = \frac{60 f_c}{z}\left(\frac{1}{2} + j - \frac{1}{\pi}\tan^{-1}\left(\frac{\lambda_{\mathrm{Im}}}{\lambda_{\mathrm{Re}}}\right)\right)^{-1} \tag{22}$$

The stability lobe diagram is obtained by plotting spindle speed $\tilde{N}$ versus the depth of cut $\tilde{a}_{\lim}$ values for each chatter frequency (the minimum at each spindle speed is selected to define the stability boundary). In this analysis, the valid chatter frequencies are not limited to those corresponding to negative real values of the oriented FRF but also cover the full range of FRF_{orient}.

In summary, Altintas and Budak developed a step-by-step procedure to create SLDs:

a. Choose a chatter frequency around a dominant mode from the transfer function.
b. Solve the eigenvalue.
c. Calculate the critical cutting depth.
d. Calculate the machine spindle speed at stability lobes, j, where $j = 0, 1, 2\ldots$.
e. Repeat the above procedure for chatter frequencies around dominant modes in the transfer function.

Faassen et al. (2003) proposed a two-dimensional dynamic model of the milling system to be used for the purpose of stability analysis. Their model was built on constants derived from dedicated experiments and used to generate the stability lobes. Furthermore, they utilized the method of D-partitioning to assess the stability of this equilibrium point. The D-partitioning method was used earlier by Stépán (1989, 1998) to investigate the milling process stability in a single-degree-of-freedom, single-mode milling model. D-partitioning uses the criterion that the equilibrium point of a system, described by a linear, autonomous-delay differential equation, is asymptotically stable if and only if all the roots of its characteristic equation lie in the open left-half of the complex plane. The characteristic equation of the model (Faassen et al., 2003) is given by

$$\det\left(\underline{H}_{uF}^{-1}\left(\frac{S}{\tau}\right)-a_p\underline{K}(1-e^{-s})\right)=0 \tag{23}$$

where det() stands for determinant, and $\underline{K}$ is a constant matrix.. A new complex variable S is introduced, where $S = s\tau$. This equation is used to determine the values for the parameter depth of cut a_p for which at least one pole lies on the imaginary axis ($s = i\omega$). Using the fact that equation (23) is derived, with $H_{xy} = H_{yx} = 0,$ and $S = i\omega^*$, with $\omega^* = \omega\tau$, which corresponds to $s = i\omega$, this transforms to

$$a_0 a_p^2 + a_1 a_p + 1 = 0 \tag{24}$$

where

$$\left.\begin{aligned} a_0 &= (1-\cos\omega^* + i\sin\omega^*)^2 H_{xx}(\omega^*)H_{yy}(\omega^*)\left(k_{xx}k_{yy} - k_{xy}k_{yx}\right) \\ a_1 &= -(1-\cos\omega^* + i\sin\omega^*)(k_{xx}H_{xx}(\omega^*) + k_{yy}H_{yy}(\omega^*)) \end{aligned}\right\} \tag{25}$$

The axial depth of cut as a function of ω^*, and $a_p(\omega^*)$ can then be found by

$$a_p(\omega^*) = \frac{-a_1 \pm \sqrt{a_1^2 - 4a_0}}{2a_0} \tag{26}$$

The critical axial depth-of-cut $a_{p_{crit}}$, with respect to stability, is defined as the depth-of-cut a_p in the parameter set defined by $\{a_p(\omega^*) : \mathrm{Im}\, a_p(\omega^*) = 0 \Lambda\, \mathrm{Re}\, a_p(\omega^*) > o\}$, for which $\left|\mathrm{Im}\, a_p(\omega^*)\right|$ has its minimum value, as shown in Figure 7, since for $a_p = 0$, all poles are in the open left-half of the complex plane when all modes of the machine dynamics are damped, which is always the case in practice. The value for ω^* for which this occurs is the dimensionless chatter frequency $\omega^* = \omega_c^*$. The real-chatter frequency that corresponds to the dimensionless-chatter frequency is $\omega_c = \omega_c^* / \tau$.

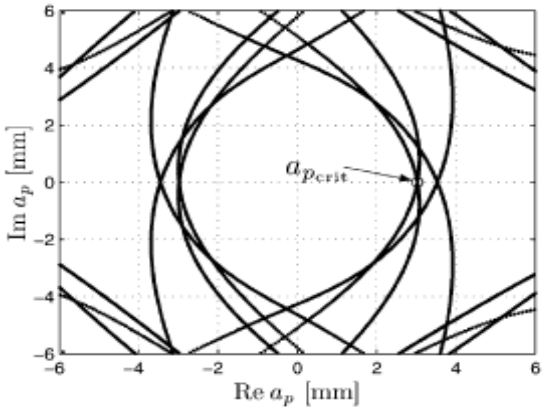

Figure 7. D-partitioning diagram for a spindle speed of 25,024 rpm (Faassen et al., 2003).

In summary, Faassen et al. (2003) presented the following procedural steps to use the D-partitioning method to find the chatter boundary in terms of critical axial depth of cut a_p for the specific spindle-speed value. These steps begin with choosing a certain spindle speed N to primarily determine the delay time $\tau = \frac{60}{zN}$ as a factor, where z is the number of teeth on the cutter. The steps given in the procedure are as follows:

a. Choose a certain spindle speed N, and calculate the delay factor (τ).

b. Choose a proper domain for ω^*.

c. Substitute $S = i\omega^*$ in the characteristic equation.

d. Solve for axial depth of cut, a_p. Now, $a_p(\omega^*)$ is known, but $a_{p_{crit}}$ still has to be found.

e. Let $\omega^* = \omega_C^*$, where $\left|\mathrm{Re}\, a_p(\omega^*)\right|$, in the parameter set defined by $\left\{a_p(\omega^*) : \mathrm{Im}\, a_p(\omega^*) = 0 \wedge \mathrm{Re}\, a_p(\omega^*) > 0\right\}$, has its minimum value. By scanning the positive real axis, it is the point where a *D*-curve crosses the real axis for the first time.

f. Calculate the chatter frequency $\omega_C = \omega_C^* / \tau$.

g. Repeat all steps for different spindle speeds, *N*.

In the second step of this procedure, a choice for the domain of ω^* should be made, such that ω_c^* lies in this domain. For a milling model, in which the lowest angular eigenfrequency of the machine dynamics is denoted by ω_l and the highest eigenfrequency by ω_h, a suitable choice for this domain would be $0.5\omega_1\tau < \omega^* < 1.5\omega_h\tau$.

2.1.4 Methods Used to Validate Model

The common methods used for validation were cutting tests. Tlusty's model considered making multiple cuttings to cover the most characteristic machining operations for the given type of machine tool, with the emphasis on operations that are critical to chatter. The frequency of chatter was verified during the cutting test, and the shape corresponding to one of the natural frequencies closest to the chatter frequency was measured separately after the cutting tests.

Cutting tests for the model by Altintas and Budak (1995) were performed on milling operations. Measured values from the tests were compared with the reconstructed transfer functions, which would indicate the accuracy of the identified modal parameters. Then, the modal parameters were used to simulate the stability lobes for milling an Al-7075 workpiece.

Validation for the model by Faassen et al. (2003) was performed by making a series of cuts on an Al-6082 workpiece on a Mikron HSM 700 milling machine. This was carried out by selecting an initial depth of cut for every spindle speed in order to eliminate the occurrence of chatter during the milling process.

A common experimental setup was used to detect the presence of chatter for all models. This program was made to scan the sound of the cutting process and measure the sound signals at a certain frequency. The frequency at which the energy level exceeds the threshold level was marked as a chatter frequency. Comparison of the chatter models is shown in Table 1.

TABLE 1

CHATTER-PREVENTION MODELS

	Tlusty (1965, 1986)	**Altintas and Budak (1995, 1998)**	**Faassen et al. (2003)**
Methods	Average tooth angle method using simplification assumptions: machine vibratory system linearity, constancy of variable components' cutting force direction, and its dependency only on vibration in the direction of the normal to the cut surface.	Fourier series approach, similar to Tlusty, which approximates time-dependent cutting forces by average value.	Spindle-speed-dependent model and generation of D-partitioning graph to detect critical depth of cut.
Advantages	Provides procedures to detect chatter frequency and create stability lobe diagrams for machine tool designers and users	Provides procedures to detect chatter frequency and create stability lobe diagrams for machine-tool users for low-speed machining.	Detects the critical depth of cut for a single high speed.
Limitations	Simplification assumptions that include a circular tool cutting path and a neglected cutting-edge helix.	Cutting-edge helix considered to be zero and neglected in the dynamic analysis.	Circular tool cutting path and a zero-angle cutting edge helix neglected in the dynamic analysis.

2.2. Rapid Prototyping and Applications for Dynamic Testing

Rapid prototyping is a technology used for processes in order to manufacture models directly from a three-dimensional (3D) computer-aided design (CAD) model through a quick, automated, and highly flexible process (Noorani, 2005). Examples of RP processes include stereolithography, selective laser sintering (SLS), fused deposition modeling (FDM), laminated object manufacturing (LOM), and three-dimensional printing (3DP), to name a few.

RP is a fast process and uses the additive principle of manufacturing by constructing the model layer by layer. It has greatly affected product development during design and manufacturing. Dulieu-Barton and Fulton (2000) indicated that RP has reduced development costs by 40% to 70% and the time to market by as much as 90%.

2.2.1. Stereolithography

Stereolithography is an RP technology, a laser-based layer-by-layer additive process, used to create three-dimensional structures by scanning a laser beam over a photocurable resin, causing the liquid to polymerize into a solid. This process requires neither masking nor special tooling.

Dulieu-Barton and Fulton (2000), Hague et al. (2004), Chockalingam et al. (2006), Mansour et al. (2007), and others have indicated that SL is a well-established technique for RP across various industry sectors. Liu et al. (2004) also pointed out that among all of the techniques, stereolithography is a fast, stable, maskless, and layer-by-layer additive process capable of building 3D, high-aspect-ratio, and lightweight micro-scale and meso-scale structures with high accuracy, i.e., achieving fabrication tolerance as small as 0.187% for three-dimensional high-frequency components.

The principle behind the stereolithography apparatus (SLA) process is shown in Figure 8 (Usher et al., 1998). SL parts are built from a photocurable liquid resin that cures when exposed to a laser beam through a polymerization process that scans across the surface of the resin. Then, the building of the part is performed layer by layer so that each layer is scanned by an optical scanning laser and controlled by an elevation mechanism, which descends at the completion of each layer. The process repeats until the required part is completed. The building process ends after completing the post-curing process at high-intensity ultraviolet radiation. The post-curing

process is dependent on the specific SL material in order to increase the mechanical properties of the produced part.

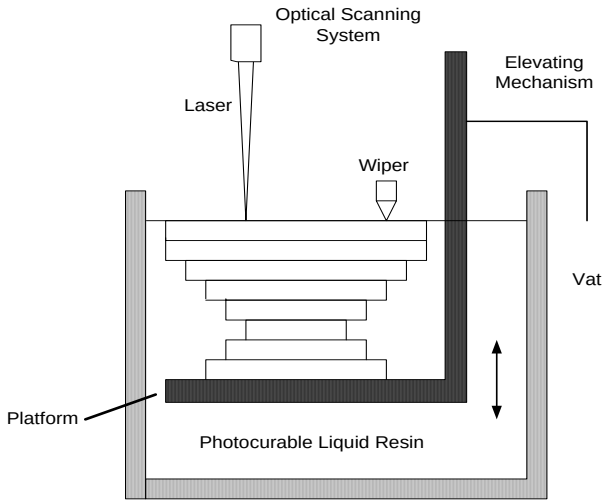

Figure 8. Working principles of SLA process (Usher et al., 1998).

.

According to Noorani (2005), the first step in RP is the creation of a CAD solid model that is fully closed and water-tight. This solid model is developed using a CAD software package. The CAD model is then saved and converted to an STL format, a file format first introduced by 3D Systems to support the stereolithography process. This file format represents the virtual CAD model of the object to be prototyped as a collection of triangular facets. These triangular facets describe a polyhedral approximation of the object's surface when taken together, that is, a polyhedral approximation of the boundary between material and nonmetal. An STL format is nothing more than a list of x, y, and z coordinate's triplets that describe a connected set of triangular facets. It also includes the direction of the normal vector for each triangle that points to the outer surface of the model. Tessellation is the process of approximating a surface by triangular facets. More tessellation involves more refinement of surfaces and solid models. The CAD STL file interface performs surface tessellation and then outputs the facet information to either a binary or ASCII STL file format.

STL file slicing is performed using pre-processing software such as 3D Lightyear. Using this software program, a user can fine-tune the dimensions, position, and orientation of the model. The position and orientation of the part in the resin bath may affect the mechanical properties and dimensional accuracy of the end part, and it is necessary to identify the orientation that best fits the requirements. Depending on the building technique requirement, the preprocessing software program slices the STL model into layers from 0.01 mm to 0.70 mm thickness. The more complex the object, the more the number of triangles required and, thus, the larger the file that makes up the CAD model as well as the support structure for the part. The sliced object is now saved as an ASCII STL file that the RP computer recognizes (Noorani, 2005).

The part is then transferred to the RP computer, and the stereolithography apparatus runs until the part is completed. The SLA builds one layer at a time and is fairly autonomous, with little human intervention. The final step is post-processing and consists of part removal, cleaning, post-curing, and finishing. This step involves manual operations, which an operator does with extreme care; otherwise, the part may be damaged and have to be prototyped again. Part removal and cleaning involves taking the prototype out of the SLA machine and removing the excess material. Post-curing of the part is needed to complete the solidification process and to improve the mechanical properties of the prototype. It is carried out in a specially designed apparatus using ultraviolet (UV) radiation. Part finishing involves basic cleaning, such as sanding or machining, to remove additional material (Noorani, 2005).

2.2.2. Stereolithography and Applications for Dynamic Testing

In recent years, RP technology has been successfully utilized during product development and early process-design stages. Dornfeld (1995) developed experimental models that were built

from stereolithography polymers with satisfactory material properties for use in direct dynamic testing. He performed the basic cantilever beam test on three types of SL materials along with traditional plastic, steel, and aluminum materials for impact excitation. He determined that the consistency of all modal frequency ratios for the aluminum and SL model beams demonstrates that the SL model beams behave dynamically according to their root E/ρ ratios. A different impact test related to scaled models of turbine blades was also carried out to determine the effect of scaling. He observed that model frequencies are inversely proportional to model scales, and that model shapes and frequencies can be determined simply and very accurately. He then concluded that SL models have been shown to have satisfactory material properties for use in direct dynamic testing.

Dornfeld finally introduced the use of scaled models, from a structural dynamics point of view of the resonant frequencies of models, which is related to true component frequencies and used to predict natural frequencies of products. The equation for this given by

$$\frac{f_{structure}}{f_{model}} = \frac{Size_{structure}}{Size_{model}} \frac{\sqrt{(E/\rho)_{structure}}}{\sqrt{(E/\rho)_{model}}} \tag{27}$$

where E is the modulus of elasticity, f is frequency, and ρ is density. Materials are assumed to be isotropic, elastic, and homogeneous.

Mahn and Bayly (1998) examined SL models as a tool for the prediction of the natural frequencies of prototype aluminum parts by impact testing. They used the free-free boundary condition to perform impact testing on SL models to predict the natural frequencies of simple shapes of aluminum. Their study used two SL materials: epoxy-based SL-5170 and acrylic-based SL-5149, with beam dimensions of 203.20 mm in length, 25.5 mm in width, and 6.35 mm in height. They considered three orientations, as shown in Figure 9, to determine if the build

process introduced anisotropy. Ten beams were built straight up from the platform for the Z orientation, laid directly over the platform for the Y orientation, and placed on their side for X orientation. They noted errors caused by deviations in the build and residual support structure.

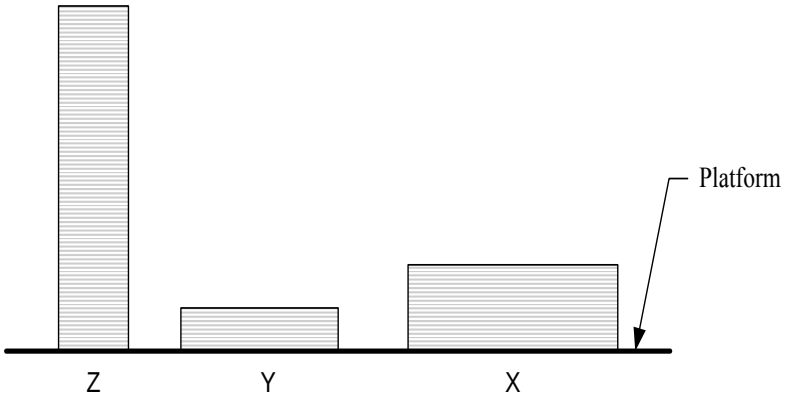

Figure 9. Three different orientations (Z, Y, X) of SLA platform beam (Mahn and Bayly, 1999).

Mahn and Bayly concluded that the SL acrylic-based material resulted in the largest deviations from the normal dimensions and proved difficult to work with. From an orientation point of view, there is noticeable deviation in the beams built, particularly, in the X direction. The beams bowed as they were post-cured, except one beam was found acceptable for testing. The SL epoxy-based beams with Y and X/Z orientations, as shown in Figure 10 were selected and built for study. It was then discovered that the structures in the X and Z orientations were identical.

All selected models were tested within two weeks of being built. The sampled frequency range of 0-1600 Hz allowed for analysis of the three modes. They observed that testing revealed that the SL material is approximately isotropic and linear, and its material properties do not vary significantly with cure time. They concluded that SL models are useful tools for the prediction of natural frequencies.

Figure 10. Square plates built in two different orientations (Mahn and Bayly, 1999).

CHAPTER 3

DISCUSSION AND RESEARCH MOTIVATION

Continued research and innovation is needed to fulfill the increasing requirements in high-speed milling for quality, reduced cost, fast delivery, and customer satisfaction. In general, the literature review of machining system dynamics provides approaches from a theoretical point of view. Multiple assumptions were made that would decrease confidence in results and thereby ignored consideration of the actual geometry of the cutting tool in the machining system. Three models have been developed to prevent chatter, and their related procedures create a stability lobe diagram so that stable cutting parameters can be determined. However, all of them were constrained with theoretical assumptions that mask the reality of the actual tool condition in the machining system.

The underlying simplifying assumptions made by Tlusty (1965, 1986) to generate the SLD were as follows: linear vibratory system of the machine, constant direction of the variable component of the cutting force, dependency of the variable component of the cutting force only on vibration in the direction of the normal to the cut surface, the straightness of the cutting tooth with zero angle of helix, and the circularity of the tool cutting path. Models by Altintas and Budak (1995, 1998) and Faassen et al. (2003) assumed that the cutting tooth path for milling is circular. Faassen (2007) pointed out that the real tool path is trochoidal, resulting from a combination of the cutter rotation and its translation in the feed direction. All three models assume that the cutting edge helix is zero by ignoring the cutting tool geometry. This raises a very important concern: that the cutting edge is typically ground with a helical profile around the

tool periphery with a constant helix angle and other geometries such as rake angle, clearance angle, etc., on solid-body end mills.

All the three models used impact testing to obtain FRF measured data to define the modal shapes, natural frequencies, stiffness, and damping coefficients for stability analysis and thereby to create the SLD graphs. However, all of them showed differences in their approaches. Tlusty (1986) assumed the average tooth angle method in addition to simplification assumptions. Altintas & Budak (1995, 1998) used a Fourier series approach, similar to that of Tlusty, in order to approximate time-dependent cutting forces by average value. Faassen et al. (2003) used a spindle-dependent approach, i.e., the D-partitioning method to find the critical depth of cut at each spindle speed related to the tooth-passing period and then to detect chatter frequency.

Each model provided procedures to detect chatter frequency in high-speed milling operations and then to create SLD graphs. The model by Tlusty (1986) is a frequency-based model and is used to identify a procedure that enables engineers to design stable machine tools and machine tool users. The model by Altintas and Budak (1995, 1998) is also a frequency-based model and provides a procedure for machine-tool users. The model by Faassen et al. (2003) is a spindle-speed dependent model and provides a procedure to generate D-partitioning graphs for users of milling machines.

Limitations indicated on the models simplify the machine dynamic analysis through assumptions. The modified models by Tlusty (1986), Altintas and Budak (1995, 1998), and Faassen et al. (2003, 2007) do not include the cutting-edge helix angle and cutting geometry in the analytical model but simply assume a zero-angle helix due to the complexity of the tool in the traditional analytical modeling. This condition may trigger failure in the prediction of the stability limit of a structure in the machining system dynamics.

Advancement in technology raised the need for rapid prototyping technology in various industries. Stereolithography is a rapid-prototyping method, which is used primarily to display the three-dimensional geometry of designed parts. As mentioned previously, Dulieu-Barton and Fulton (2000), Hague et al. (2004), Chockalingam et al. (2006), Mansour et al. (2007), and others have indicated that SL is a well-established technique for RP across various sectors of industry. Liu et al. (2004) indicated that stereolithography is a fast, stable, maskless, and layer-by-layer additive process capable of building 3D with high accuracy, i.e., achieving fabrication tolerance as small as ~0.19% for the three-dimensional high-frequency components.

Dornfeld (1995) was the first to utilize SL models for dynamic testing. His study developed experimental models built from stereolithography polymers and recognized that the SL model beams behave dynamically according to their root E/ρ ratios. He also observed the model frequencies to be inversely proportional to model scales. He then concluded that SL models have been shown to have satisfactory material properties for use in direct dynamic testing.

Mahn and Bayly (1999) examined the application of SL models to predict the natural frequencies of the aluminum material. They used two types of SL polymers: acrylic-based and epoxy-based. They used three building orientations such as X, Y, and Z to observe the effect of orientations for anisotropy and linearity. They found that the acrylic-based SL material showed much dimensional variance, particularly, in the X direction. Then, they selected epoxy-based SL material to continue with the experimentation. They observed that the testing revealed the SL material is approximately isotropic and linear, and its material properties do not vary significantly with cure time. Then, they concluded that SL models are useful tools for the prediction of natural frequencies of aluminum materials.

In summary, it is apparent that traditional models are used to prevent chatter generation by detecting chatter through creating stability limits. However, the limitations due to the simplifying assumptions ignore the presence of the cutting tool geometry and may mask areas of chatter generation. On the other hand, it has become evident that SL models have shown satisfactory results in direct dynamic testing and are also useful tools for the prediction of natural frequencies. Since SL models display the actual three-dimensional geometry of the designed part, there would be no hidden geometry during their prediction. An important revelation of the literature review is the need for tooling and cutting-tool design research to implement this concept in machining systems.

CHAPTER 4

RESEARCH OBJECTIVES AND PROCEDURE

This research aimed at addressing not only the core limitations in the cited analytical models, as explained in Chapter 2, but also the utilization of SL models in predicting the cutting-tool design parameters. Research efforts have placed special emphasis on the design of end mills as the most commonly used cutting tools in milling operations. This approach was expected to predict the dynamic characteristics of the machining system as a whole, including the spindle, tool holder, and end mill.

To achieve this end, the following three objectives were identified:

a. To demonstrate the ability to model the dynamic characteristics of the tooling system using SL models.
b. To quantify the effect of changes in the stereolithography process and tool design parameters on the predicted dynamics characteristics.
c. To develop a methodology for determining the cutting tool design parameters required to achieve desired performance levels utilizing SL models.

4.1 Demonstration of Modeling Capability Using SL Models

An initial investigation of this research focused on the usefulness of SL models in predicting the dynamic characteristics of carbide barstock. The approach began with selecting a tool grade carbide barstock and constructing its SL models. The barstock was first CAD modeled, and then its SL model was built following the process shown in Figure 11.

The barstock material (H10F) chosen for testing was ¾ inch in diameter and 5 inches long, and the unscaled SL models were built using three orientations: X, Y, and Z. The actual physical dimensions were measured two weeks after construction, and the results are shown in

Table 2. Five SL models were built for each orientation, and 10 measurements were taken from each orientation.

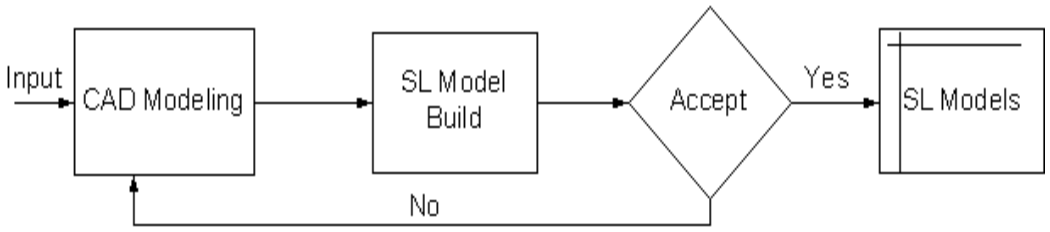

Figure 11. SL model construction process.

TABLE 2

DIMENSIONAL AND PHYSICAL ACCURACY OF SL MODELS

SL Model Build Orientation	**Diameter (in)**		**Weight (lb)**		**Calculated Density (g/cc)**	
	Average	*Stdev*	*Average*	*Stdev*	*Average*	*Stdev*
X	0.7480	0.0068	40.453	0.044	1.127	0.020
Y	0.7486	0.0050	40.406	0.062	1.123	0.015
Z	0.7446	0.0025	39.975	0.059	1.123	0.007

The dimensional and physical accuracy data in Table 2 shows that a slight difference was observed between the sizes of the three build orientations. The standard deviation for the calculated density showed the lowest value as compared to the X and Y build orientations. A general two-factor factorial design was used to perform to check for its level of significance. Factor A: orientation has three levels X, Y, and Z, and Factor B: parameter has two levels, diameter (inch) and calculated density (g/cc) and the response is based on standard deviation (stdev). Weight is not considered in the levels since it is included in the calculation for density.

The analysis of variance (ANOVA) for this experiment was performed using Deign Expert version 6.0.6 software and the results were shown in Table 3.

TABLE 3. Analysis of Variance: RESULTS FOR ORIENTATION

Source	*Squares*	*DF*	*Mean Square*	*F*	*P-value*	
Model	0.00021	3	7.0E-05	7.109	0.126	Not significant
A, Orientation	0.00007	2	3.7E-05	3.824	0.207	
B, Parameter	0.00013	1	1.3E-04	13.680	0.066	Significant for P-value < 0.01
Residual	0.00002	2	9.8E-06			
Cor Total	0.00023	5				

The P-value for B, parameter indicated that it is significant at alpha 10% level. The standard deviation was plotted for B, parameter and the SL model with Z orientation exhibited the lowest value of standard deviation as shown in Figure 12. The following section shows the dynamic characteristics of the tool and SL models.

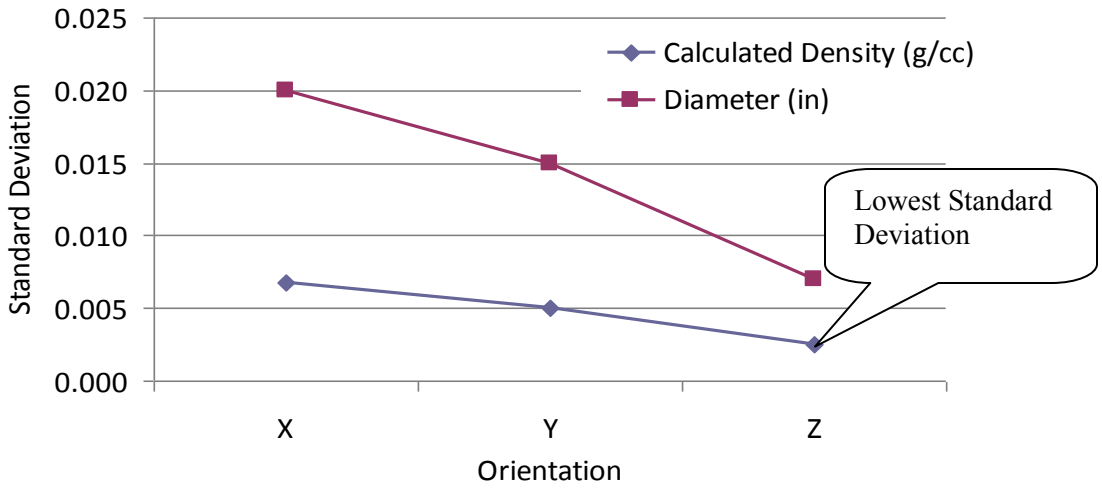

Figure 12. Evaluation of the SL model for build orientation

4.2 Dynamic Characteristics of Carbide Barstock and SL Models

To account for the relationship between the actual tool material and the SL model, each material property needs to be given. The carbide tool material chosen for the experiment was H10F and SL resin used was 11120 WaterShed™, which is a low-viscosity liquid photopolymer that produces strong, tough, water-resistant, ABS-like SL models. Material properties include the modulus of elasticity and density of the tool and model. The material properties of the parts in the experiment are shown in Table 4. A list of the properties of the 11120 WaterShed™ resin is included in Appendix F.

TABLE 4

MATERIAL PROPERTIES

Material	**Elastic Modulus (E), MPa**	**Poisson's Ratio (ν)**	**Density (ρ), g/cc**
SL Model 11120 WaterShed™	2,650–2,880 (4.0100E + 05 psi)	0.35	1.120–1.123 (1.0481E – 04 lbm/in^3)
Carbide Tool H10F	552,000–650,000 (8.4120E + 07 psi)	0.22	14.5–14.6 (1.3509E – 03 lbm/in^3)

Using the Bernoulli-Euler theory (Thomson, 1993; Craig and Kurdila, 2006) for theoretical free-free vibration of the uniform beam, the following equation was used to estimate the natural frequency of the barstock:

$$\lambda^4 = \omega^2 \frac{\rho A}{EI} \tag{28}$$

where λ is the eigenvalue (natural frequencies), ω is the natural rotational frequency, EI is vertical bending stiffness, ρ is mass density, and A is the cross-sectional area of the beam.

Further explanation of Bernoulli-Euler theory can be found in Appendix C. The natural frequencies for mode shapes of beam configurations are given by

$$f_r = \frac{(\lambda_r L)^2}{2\pi L^2}\sqrt{\frac{\mathrm{EI}}{\rho A}} \tag{29}$$

where:

$r = 1, 2, 3\ldots$	Mode shapes (1st mode, 2nd mode, 3rd mode…)
$(\lambda_1 L)^2 = 22.4$	First mode coefficient free-free beam
$A = \frac{\pi d^2}{4}$	Cross-sectional area of barstock
$I = \frac{\pi d^4}{64}$	Area moment of inertia
$d = ¾"$	Diameter of barstock
$L = 5"$	Length of barstock
f_{H10F}	Fundamental frequency of H10F carbide barstock
f_{11120}	Fundamental frequency of SL model 11120 WaterShed™ blank

Calculations using equation (29) resulted in the estimation of

$$f_{H10F} = 6{,}672\ Hz \quad \text{and} \quad f_{11120} = 1{,}654\ Hz.$$

The finite element method (FEM) is the most inexpensive method and reliable way of comparing test data with an analytical model in the product design and development stages. Therefore, the finite element (FE) model is also used to obtain natural frequencies of vibration. Once the modes are available, their orthogonality allows the linear response of the structure to be constructed as the response of a number of single-degree-of-freedom systems, which provide useful insight into the structure's dynamic behavior, as shown in Figure 13. Accordingly, in this research, the FE method utilized for free-free vibration excitation used number of nodes =

26,952, number of elements = 25,972, number of modes = 5, 8-node 24-DOF brick elements, and number of parts = 1, to achieve more accurate results.

Figure 13 is a pictorial representation of the FE analysis results. The natural frequency at the first mode for the H10F carbide barstock was found to be 6,306 Hz, as shown in Figure 13(a), and the natural frequency at the first mode for the SL model was 1,561 Hz, as shown in Figure 13(b).

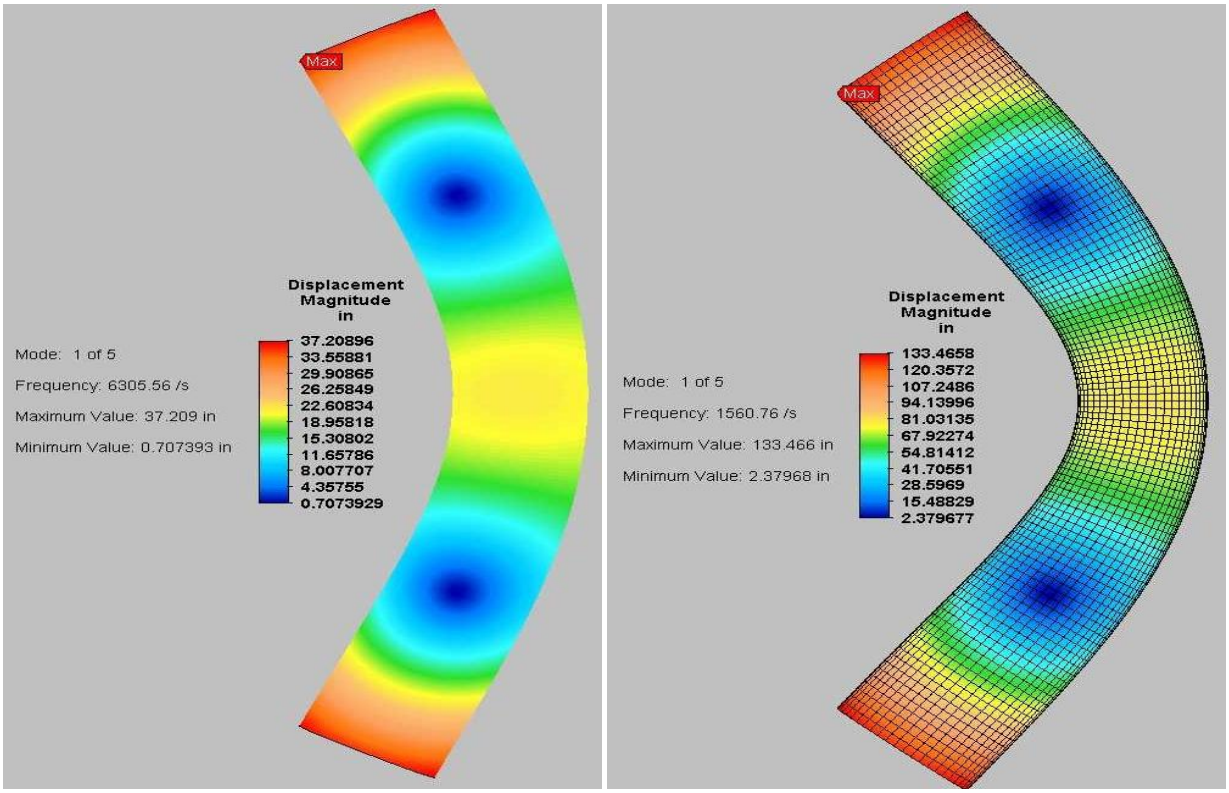

(a) (b)

Figure 13. Free-free boundary condition: (a) FE method of H10F carbide barstock, and (b) SL model 11120 WaterShed™ blank results.

In order to demonstrate the modeling capability using an experimental method, frequency response function measurements (FRF) were taken on free-free boundary condition (FFBC) by exciting the end of the barstock with an impact hammer. The barstock was excited from the opposite end of the glued accelerometer location, and the FRF measurements were taken. The

experimental setup for the FFBC was then repeated by suspending the barstock by an elastomer band, as shown in Figure 14.

An accelerometer Model 352B10 and an impact hammer Model 086C03 by PCB PIEZOTRONICS™, and DP240-2C Quattro DSP centric signal processing hardware, and SignalCalc Ace Quattro-powered software by Data Physics Corporation were used to perform the experiments. The PCB Model 086C03 impact hammer was calibrated on June 16, 2009; measurement uncertainty (92% confidence level with a coverage factor of 2) is +/-3.8%. The PCB accelerometer Model 352B10 is calibrated on May 4, 2010; measurement uncertainty for frequency ranges: 5-9 Hz, +/-2.0%; 10-99 Hz, +/-1.5%; 100-1999 Hz, +/-1.0%, and 2-10 kHz, +/-2.5%. The Data Physics DP240-2C Quattro DSP centric signal processing hardware calibration date is June 3rd, 2010 and due date is December 3rd, 2010, and its calibration certificate number is 09N4198. All calibration certificates are located in Appendix E. The testing process included gage repeatability and reproducibility before actually beginning measuring the test products. Result of gage repeatability is 8.2%, reproducibility is 8.2% acceptable, and combined GR&R is 11.5%. These results are acceptable according to AIAG (2002) standard. The tool swayed freely after excitation, and the data was captured through the SignalCalc data analyzer.

First, the H10F carbide barstock was suspended, as shown in Figure 14, and impacted to obtain the FRF data. Five impacts were replicated three times, and a total of fifteen data points were collected. The first mode experimental modal analysis (EMA) results of the dynamic characteristics are shown in Table 5.

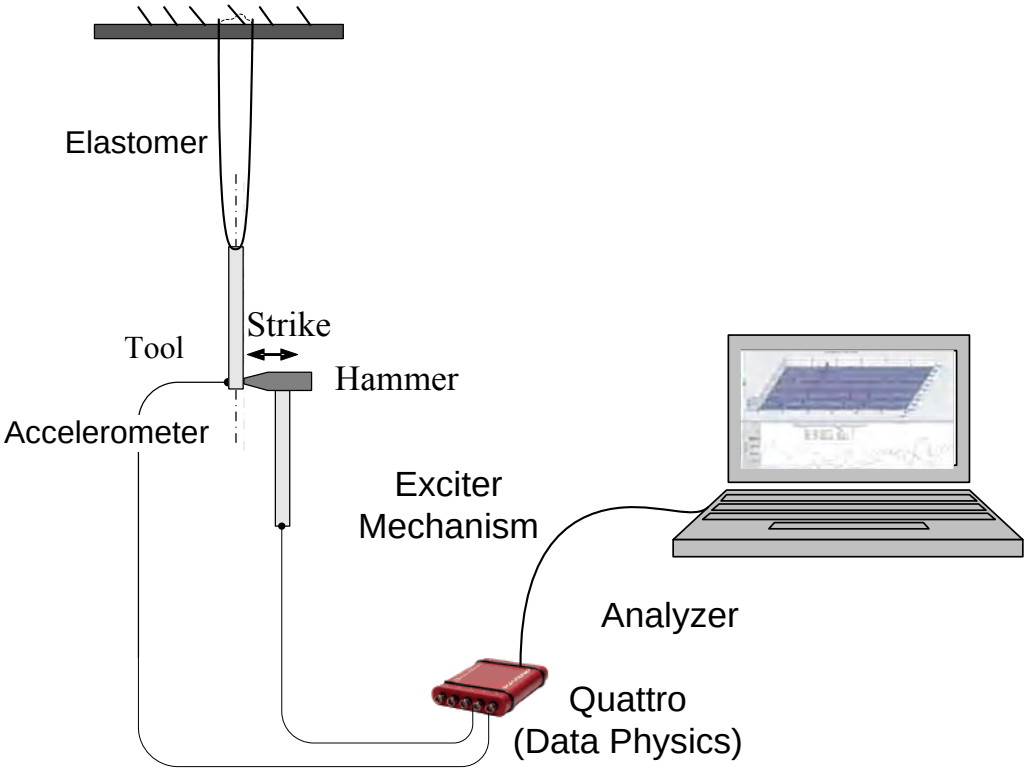

Figure 14. Experimental setup for free-free boundary condition.

TABLE 5

TEST RESULTS OF H10F CARBIDE BARSTOCKS

Peak Frequency (Hz)	**Average**	**Standard Deviation**	**Coefficient of Variation (%)**
f_1	6,195	1.6559	0.03
f_2	6,221	1.3703	0.02
f_n	6,207	1.4534	0.02

SL models were built in three orientations: X, Y, and Z. It were necessary to determine if test results of the dynamic characteristics could hold the same for the three orientations. Three samples of each orientation were used for the experiment. Five impacts were replicated three

times for each sample. So in total, 45 measurements collected. The average test results of the SL models were shown in Table 5.

TABLE 6

TEST RESULTS OF SL MODELS

Peak Frequencies (Hz)	Model Orientation	Average	Standard Deviation	Coefficient of Variation (%)
f_1	X	1,564	7.3	0.47
	Y	1,572	4.5	0.29
	Z	1,565	6.4	0.41
f_2	X	1,642	7.3	0.44
	Y	1,624	4.3	0.27
	Z	1,619	7.5	0.46
f_n	X	1,610	7.7	0.48
	Y	1,601	5.6	0.35
	Z	1,593	6.8	0.43

Test results were displayed in Table 6 for the average, standard deviation, and the coefficient of variation of the data collected. In order to check the effect the model orientation based on the peak frequencies, a general factorial two-factor design was considered. Factor A, peak frequencies has three levels f_1, f_2, and f_n; and factor B, model orientation has three levels X, Y, and Z orientations. The input factors and data are clearly displayed in Table 6. The analysis of variance in Table 7 explained that the average peak frequencies are significantly different among themselves at 95% confidence level. The analysis of variance for standard deviation as shown in Table 8 indicated that there is no significant difference in the data and hence, this explains the data collected is of good quality and consistent. On the other hand, the model orientation was

found to be not significantly different at 95% confidence level on average. It showed significant differences on the standard deviations at the same confidence level. Therefore, it was concluded that the model orientations are significantly different and the peak frequencies' showed no significant difference between standard deviations at 95% confidence level.

TABLE 7

ANALYSIS OF VARIANCE (RESPONSE: AVERAGE)
EFFECT OF MODEL ORIENTATION ON PEAK FREQUENCIES

Source	*Sum of Squares*	*DF*	*Mean Square*	*F*	*P-value*	
Model	5923.11	4	1480.8	26.707	0.0038	significant
A, Peak frequencies	5669.56	2	2834.8	51.128	0.0014	significant
B, Model orientation	253.56	2	126.8	2.287	0.2177	not significant
Residual	221.78	4	55.4			
Cor Total	6144.89	8				

TABLE 8

ANALYSIS OF VARIANCE (RESPONSE: STANDARD DEVIATION)
EFFECT OF MODEL ORIENTATION ON PEAK FREQUENCIES

Source	*Sum of Squares*	*DF*	*Mean Square*	*F*	*P-value*	
Model	12.23	4	3.058	11.074	0.0194	significant
A, Peak frequencies	0.60	2	0.301	1.091	0.4188	not significant
B, Model orientation	11.63	2	5.814	21.058	0.0075	significant
Residual	1.10	4	0.276			
Cor Total	13.34	8				

4.3 Summary of Dynamic Characteristics in Free-Free Boundary Condition

In summary, natural frequencies obtained using the analytical method (Bernoulli-Euler theory), finite element method, and experimental modal analyses were compared for a uniform barstock with a diameter of ¾ inch and length of 5 inches. Table 9 shows the EMA results that describe the dynamic characteristics of the barstock. The scale factors for all methods were calculated to show the usefulness of the SL models in predicting the natural frequencies of cutting tools using free-free boundary condition.

TABLE 9

SUMMARY OF THREE METHODS NATURAL FREQUENCIES f_n AND SCALE FACTOR

Free-Free Boundary	**H10F Carbide Tool CT Barstock (Hz)**	**11120 WaterShed SL Model (Hz)**	**Scale Factor (CT/SL)**
Analytical (Bernoulli-Euler) Method	6672	1654	4.0
Finite Element Method (FEM)	6306	1561	4.0
Experimental Modal Analysis (EMA) Impact Testing	6207	1593	3.9

Further analyses were provided in Table 10. Natural frequencies of the three methods were compared and shown to reflect the impact in percentage as related to the experimental method.

- SL Model Natural Frequencies: the analytical method (Bernoulli-Euler Theory) deviates 5.6% from the FEM and 3.7% from experimental method. The finite element method also deviates 2.0% from the experimental method.

- H10F Carbide Barstock Natural Frequencies: the analytical method deviates 5.5% from the FEM and 7.0% from experimental method. On the other hand, the finite element method deviates 1.6% from the experimental method.
- The Scale Factor: the analytical method deviates 0.1% from the FEM and 3.4% from experimental method. On the other hand, the finite element method deviates 3.5% from the experimental method.

TABLE 10

PERCENT DEVIATIONS FROM EXPERIMENT METHOD

11120 WaterShed™ *SL* *Model (Hz)*	**Analytical (Bernoulli-Euler) Method**	**Finite Element Method (FEM)**	**Experimental Modal Analysis (EMA) Impact Testing**
Analytical (Bernoulli-Euler) Method	0.0%	-5.6%	-3.7%
Finite Element Method (FEM)	-5.6%	0.0%	2.0%
Experimental Modal Analysis (EMA) Impact Testing	-3.7%	2.0%	0.0%
H10F Carbide Tool (CT) Barstock (Hz)	**Analytical (Bernoulli-Euler) Method**	**Finite Element Method (FEM)**	**Experimental Modal Analysis (EMA) Impact Testing**
Analytical (Bernoulli-Euler) Method	0.0%	-5.5%	-7.0%
Finite Element Method (FEM)	-5.5%	0.0%	-1.6%
Experimental Modal Analysis (EMA) Impact Testing	-7.0%	-1.6%	0.0%
Scale Factor percent Deviation	**Analytical (Bernoulli-Euler) Method**	**Finite Element Method (FEM)**	**Experimental Modal Analysis (EMA) Impact Testing**
Analytical (Bernoulli-Euler) Method	0.0%	0.1%	-3.4%
Finite Element Method (FEM)	0.1%	0.0%	-3.5%
Experimental Modal Analysis (EMA) Impact Testing	-3.4%	-3.5%	0.0%

This indicates that fewer percentages were exhibited with the finite element method than the analytical method with respect to the experimental method. In general, the initial study demonstrated the usefulness of SL models accurate prediction of the dynamic characteristics of carbide barstock. In the next section, the effects of changes in the stereolithography process and tool design parameters on the predicted dynamic characteristics are quantified.

4.4 Effect of Changes in Stereolithography Process and Tool Design Parameters

Earlier in the free-free boundary condition analysis of solid barstocks of carbide and their SL models, the modeling ability of the dynamic characteristics of barstocks was demonstrated. The next study dealt with the dynamic characteristics of the ¾-inch diameter solid carbide end mills and their SL models that include cutting geometry, as shown in Figure 15. The tool materials for the tools considered are H10F carbide tools. The end mill type: Ball-nose type with Diameter ¾ inch, length 5 inches, and flute length 2 inches. Two designs of the end mill were considered. The first includes cutting geometries with a helix angle of 45 degrees and a rake angle of 10 degrees, and the second with a helix angle of 35 degrees and a rake angle of 18 degrees.

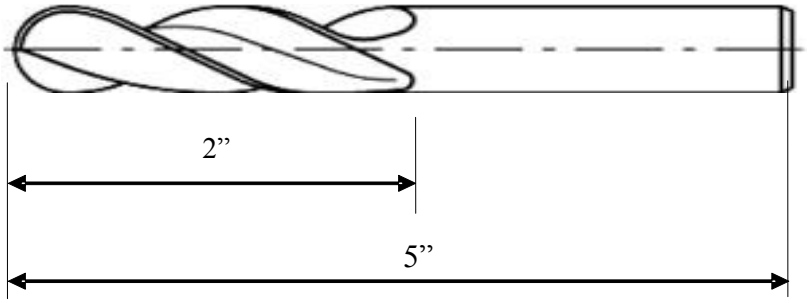

Figure 15. End mill ¾ inch in diameter and 5 inches in length.

A three-dimensional computer-aided design model was developed and transformed to the STL file format to build the SL model. The same experimental setup, shown in Figure 14, was again utilized to perform the free-free boundary condition test for the cutting tools. In this case,

two samples were built for each set of tool geometries. The test includes five impacts repeated three times for each sample. In total, 15 measurements were collected for each part. A 2^2 factorial design was applied to study the effect of changing the cutting geometry. The design summary is explained in Table 11 and the experimental data were shown in Table 12.

TABLE 11

DESIGN SUMMARY: 2 LEVEL FACTORIAL EXPERIMENTS

Factor	**Name**	**Low Actual (-)**	**High Actual (+)**	**Levels**
A	Material	SL	CT	2
B	Design	H45/R10	H35/R18	2

TABLE 12

DESIGN MATRIX FOR 2 LEVEL FACTORIAL EXPERIMENTS

Run	Factors		Responses	
	Material	Design	Average Natural frequency	Standard Deviation
1	-1	-1	1188	2.97
2	-1	1	1253	2.16
3	1	-1	5069	3.04
4	1	1	5408	1.50

The experiment was first run using the response data for the standard deviation. The analysis of variance shown in Table 13 indicated that there was no significant difference in the data at 95% confidence level. Therefore, the data was considered consistent and it would be acceptable to use the average frequency data for analysis.

When using the average natural frequency data as a response, the analysis of variance shown in Table 14 indicated that the model is not significant at 95% confidence level. There was no question that the material factor used was significantly different, and the design factor showed insignificant difference as related to its high frequency. It is possible to understand that geometry change resulted in variation in the dynamic testing. The p-value for factor B is 0.26 and the gap between the two designs of the tools shown in Figure 16 would indicate the sensitivity due to change in cutting tool geometry.

TABLE 13

ANALYSIS OF VARIANCE: STANDARD DEVIATION

Source	*Sum of Squares*	*Df*	*Mean Square*	*F-Ratio*	*P-Value*	
Model	1.48	2	0.738	5.499	0.2887	not significant
A, Material	0.09	1	0.085	0.635	0.5717	
B, Design	1.39	1	1.391	10.362	0.1917	
Residual	0.13	1	0.134			
Cor Total	1.61	3				

TABLE 14

ANALYSIS OF VARIANCE: AVERAGE FREQUENCY

Source	*Sum of Squares*	*Df*	*Mean Square*	*F-Ratio*	*P-Value*	
Model	1404.1	2	702.1	1406.1	0.0189	not significant
A	1401.5	1	1401.5	2806.8	0.0120	
B	2.7	1	2.7	5.4	0.2596	
Residual	0.5	1	0.5			
Cor Total	1404.6	3				

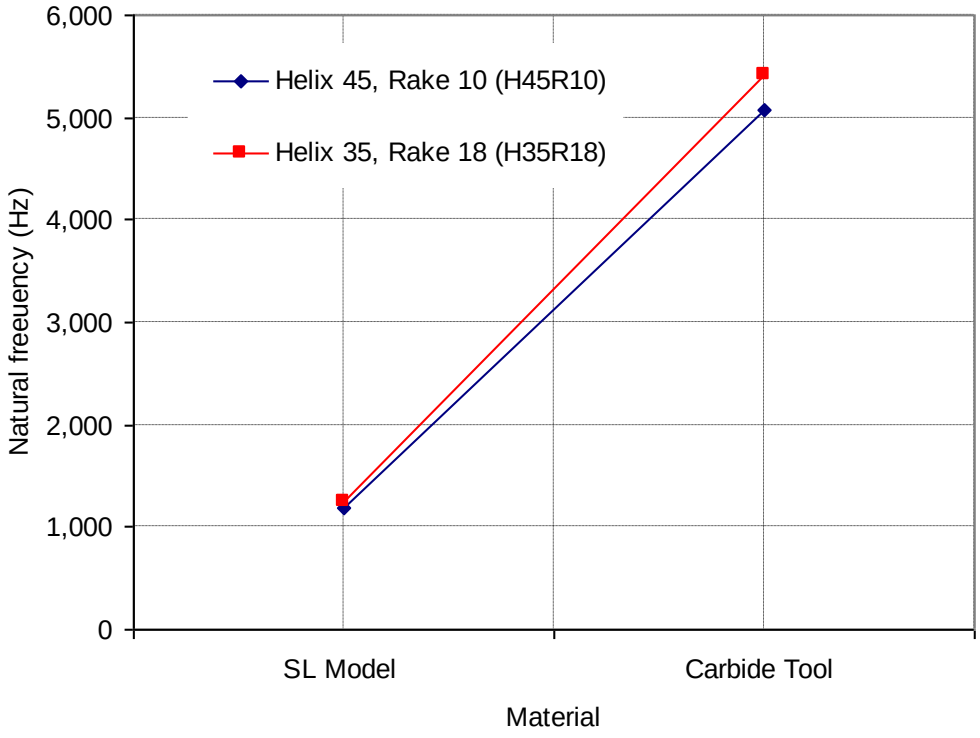

Figure 16. Effect of the cutting tool geometry change at free-free condition.

In addition, the scale ratio of the carbide tool to the SL model is equal to 4.3 for both geometries, as shown in Table 15. This indicated that both geometries have the same scaling factor in free-free boundary condition excitation. The FRF measurements conducted and the analyzed results shown in Table 15 are in agreement with the results of equation (27) by Dornfeld (1995). That is, the ratio $\frac{f_{Tool}}{f_{SL\_model}}$, calculated based on the data in Table 4, was found to be in the range of 3.83 to 4.38.

TABLE 15

DYNAMIC CHARACTERISTICS FOR END MILLS
WITH FREE-FREE VIBRATION CONDITION

Dynamic Parameters	**Natural Frequency f_n *(Hz)***			**Stiffness *k* (N/m)**		
Material / Design	**Carbide Tool**	**SL Model**	**Scale Factor**	**Carbide Tool**	**SL Model**	**Scale Factor**
Helix 45, Rake 10	5,069	1,188	4.3	2.49E+07	3.38E+05	73.7
Helix 35, Rake 18	5,408	1,253	4.3	2.80E+07	3.79E+05	73.9
Impact Ratio H35R18/H45R10	1.067	1.055		1.124	1.121	

On the other hand, the tool with helix 35/rake 18 cutting geometry showed 6% to 7% increase in natural frequencies and 12% increase in stiffness over the tool with helix 45/rake10 geometry. Therefore, it is understandable that changes in tool-cutting geometry resulted in variations in their dynamic characteristics in the free-free boundary condition excitation experiment. In this study, it became apparent that SL models are sensitive to changes in cutting tool geometry. The dynamic characteristics of end mills and the corresponding SL models can be approximated using the free-free boundary condition experiment, and can be concluded that SL models are of value in predicting their dynamic characteristics.

CHAPTER 5

CHARACTERIZATION OF DYNAMIC PROPERTIES

Experimentation using impact testing offers an analysis of the dynamic properties of the cutting-tool easily in a free-free boundary condition. For machining processes, cutting tools are clamped into a machine spindle-holder-tool and can be positioned at different overhang (OH) lengths. OH is a length or distance from the clamping position of the tool to its cutting tip end. The overhang length *x* is shown in Figure 17. However, this specific experimental model analysis deals with samples of ¾" diameter and 5 inches long from H10F barstock and the corresponding SL models.

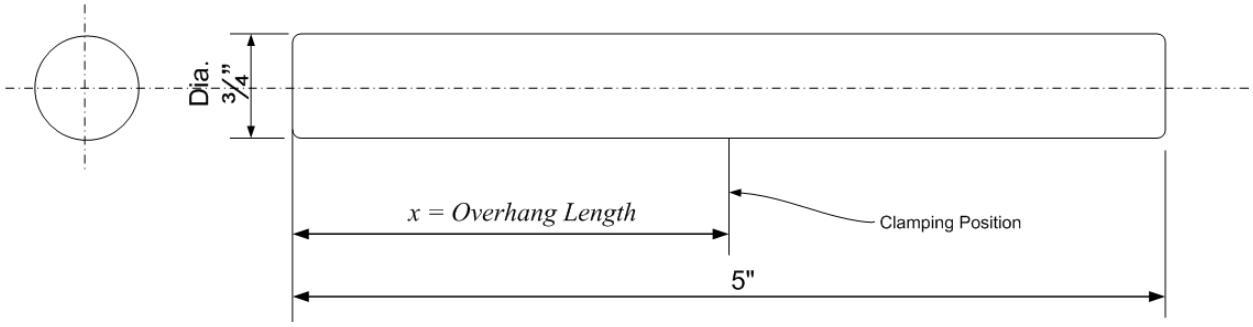

Figure 17. Barstocks clamping positions or overhang lengths (x inches)

The OH lengths considered in this section were 2.0, 2.5, 3.0, 3.5, and 4.0 inches. In order to perform experimental modal analysis, frequency response function measurements were collected for the carbide barstock and its SL model for the cited overhang lengths. The analyzed results for the OH lengths are shown in the plots in Figure 18 and explained as follows:

- As excitation occurs with increasing overhang length, the natural frequencies decrease, as shown in Figure 18(a) and (b).

- The resulting stiffness of both the carbide tool and the SL model has a similarly demonstrated decreasing trend, as shown in Figure 18(c) and (d).

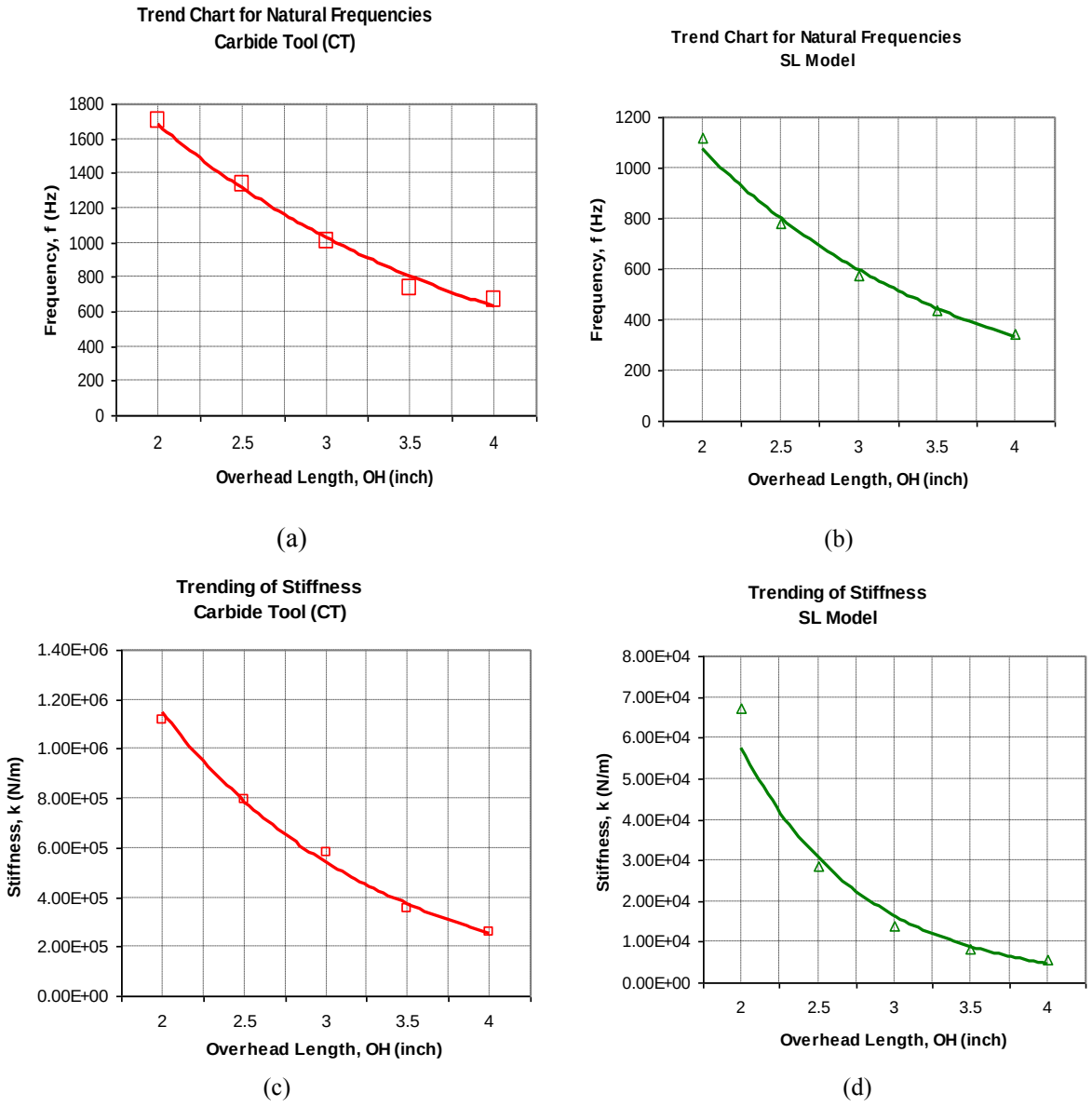

Figure 18. Characterization of carbide tool and SL model:
(a) and (b)—natural frequencies, (c) and (d)—stiffness at overhang lengths.

5.1 Boundary Condition-Based FRF Measurements

The experimental setup on a Haas CNC-VF2 milling machine is shown in Figure 19. The solid end mill was clamped at overhang length 3.0 inches from the tip end of the tool. The impact excitation occurred at the tip of the end mill, opposite to the glued-on accelerometer. The same apparatus as previously shown in Figure 14 was used for this experimental setup. Data was captured through the Data Physics Quattro signal analyzer and contained frequency peaks f_1, f_2, and f_n, at real part Re(G_{max}), Re(G_{min}), and magnitude (H) or Im(G_{min}), respectively.

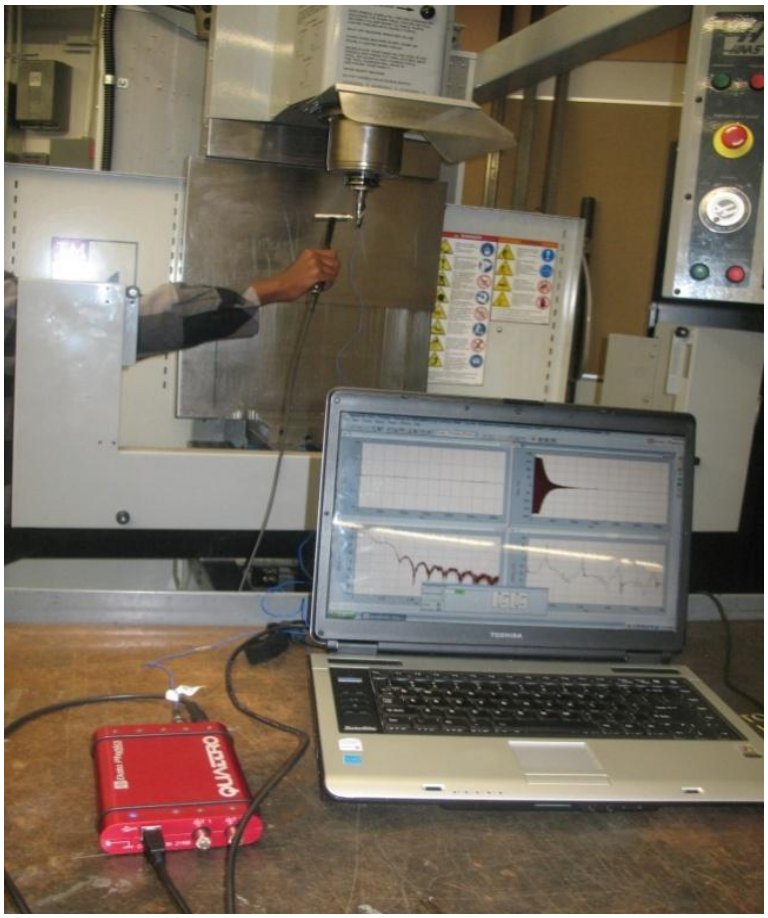

Figure 19. Experimental setup for testing using impact hammer method.

The FRF data collection in this setup actually reflects the machine spindle-holder-tool combined or the machining system's dynamic characteristics. Henceforth, the experimental

modal analysis (EMA) deals with the machining system dynamic characteristics. The overhang distance *x* on the end mill was shown in Figure 20. The peak frequencies and stiffness values at 3.0 inch-OH distance are shown in Table 16.

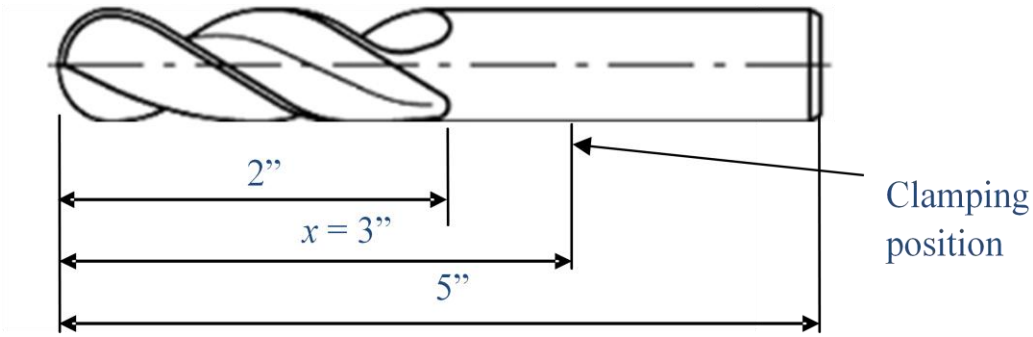

Figure 20. End mills clamping at overhang length *x* distance

Test results were analyzed using single variable analysis for each of the peak value frequencies, f_1, f_2, and f_n, of the CT H10F and its SL models at 3.0 inch-overhang length. The peak frequencies for the carbide tools and their SL models were approximately parallel to each other, as shown in Figure 21. The ratio of the H10F tool to its SL model frequencies, called the ~~–~~scale factor,” was then calculated and shown in Table 16. Hence, the scale factor, determined at *x* distance from the tip of the cutting edge to the clamping position, called ~~–~~overhang length,” helps to predict the dynamic characteristic of the intended tool.

The results, in Table 16, indicated a maximum of 1.4% error for predicting the natural frequencies f_n, and less than 1% for predicting stiffness of the machining system. Therefore, it was concluded that the scale factor obtained from this calculation would be used for predicting the dynamic characteristics of an intended tool.

TABLE 16

SCALE FACTOR OF END-MILL GEOMETRY OF SL MODEL

Geometry	Helix 35, Rake 18			Helix 45, Rake 10			Scale Factor	between % Error	
Dynamic Parameter	Carbide Tool (CT)	SL Model (SL)	Scale (CT/SL)	Carbide Tool (CT)	SL Model (SL)	Scale (CT/SL)		Helix 35, Rake 18	Helix 45, Rake 10
f_1	1410	733	1.92	1334	673	1.98	1.94	-0.7%	2.4%
f_2	1428	755	1.89	1356	696	1.95	1.94	-2.3%	0.6%
f_n	1426	747	1.91	1353	689	1.96	1.94	-1.4%	1.4%
k	2.20E+06	3.44E+04	63.99	1.46E+06	2.31E+04	63.20	63.59	0.6%	-0.6%
z	0.006	0.015	0.43	0.008	0.017	0.48	0.45	-4.8%	4.8%

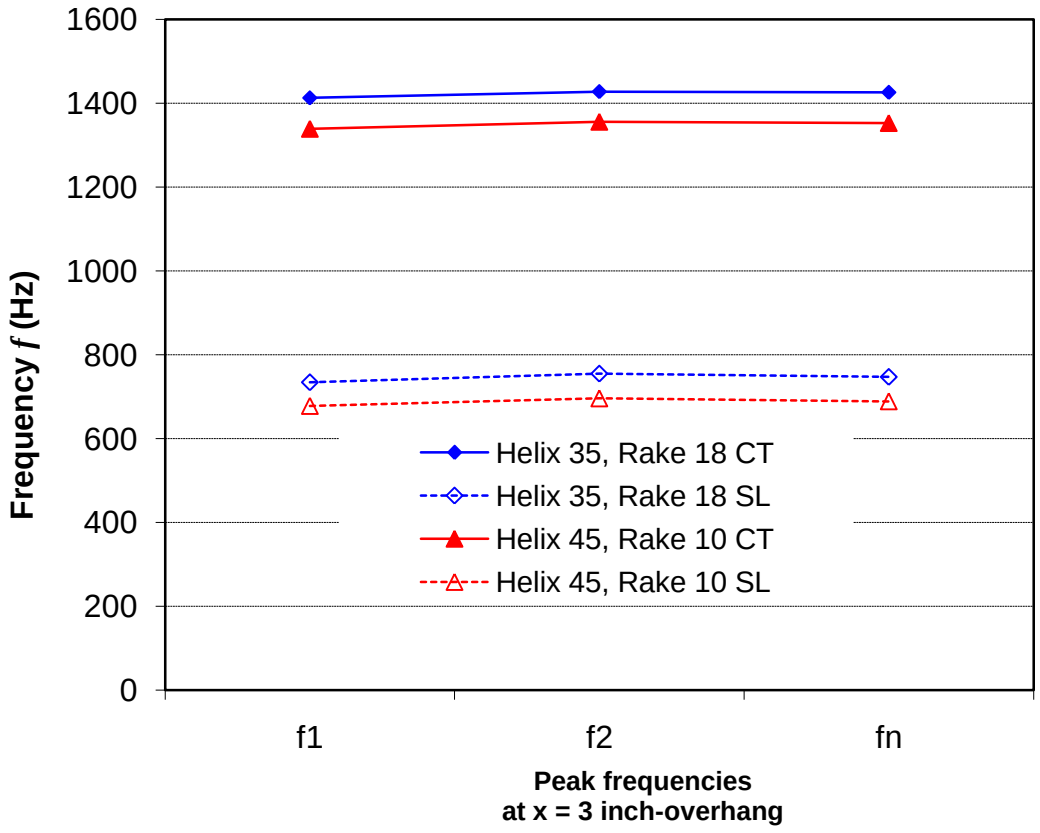

Figure 21. Tool and SL model peak frequencies at overhang length, x = 3.0 inches.

5.2 Evaluating Dynamic Characteristics of Tool in Machining System

This section involves a combination of the machine spindle, tool holder and cutting tool. As described in section 5.1, the dynamic characteristics for the two selected end mills with cutting geometry of helix angle 35 degree and rake angle 18 degree, and helix angle 45 degree and rake angle 10 degree were determined. Their scale factor was also identified for x = 3.0 inch-overhang distance. In order to evaluate these tools in machining system, it is necessary to primarily reproduce the real and imaginary parts of the equation of motion plots for single degree of freedom. Then, the stability lobe diagrams (SLDs) will be generated to evaluate the tool design parameters such as: the axial depth of cut and spindle speed. Stability lobe diagrams are meant to create boundaries that identify stable and unstable cutting regions separated by lobes of stability as a function of axial depth of cut and machine spindle speed.

The first step to creating an SLD is to reproduce the real and imaginary parts of the single degree of freedom equation (11) for demonstration. The real part has maximum and minimum points from an FRF magnitude point of view. The maximum point indicates the minimum frequency f_1, while the minimum peak point, which is negative, indicates the maximum frequency f_2 (chatter). The imaginary part has only one peak point (negative) where there is natural frequency f_n. Chatter occurs between natural frequency and maximum frequency (highest chatter). The illustration is provided in Figure 22 showing the real and imaginary part plots, and used to create SLDs. The real part plot indicates the chatter and instability frequency regions.

Additional inputs such as: material type and its specific cutting power, immersion angles, and cutting force angles are required to create the SLD. From Table 16, the dynamic characteristics of the end mills at 3.0 inch-overhang distance were obtained. Material → Al-7075-T6 was selected and its specific cutting power, k_s = 850 N/m^^2, entry angle = 0 degree and

exit angle = 180 degree. As shown in Figure 23, the real and imaginary parts were plotted for the actual end mill with helix angle 35 degree and rake angle 18 degree.

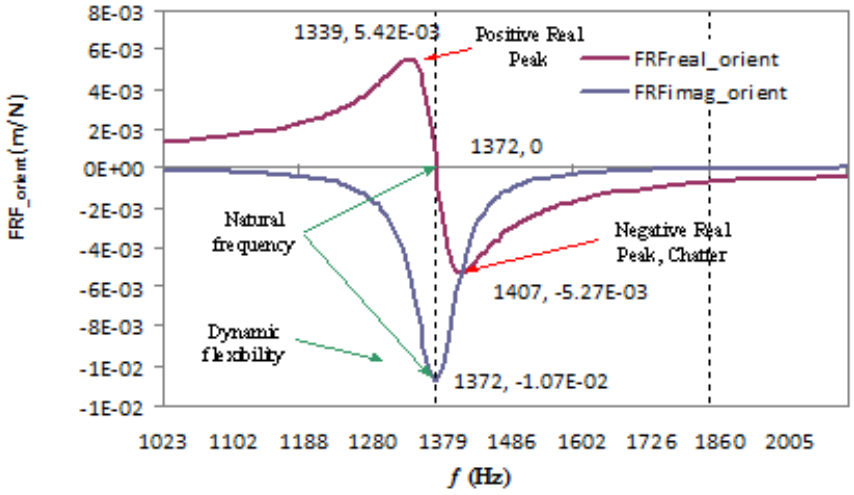

Figure 22. Real and imaginary parts FRF measured at x=3.0 inch-OH (Example).

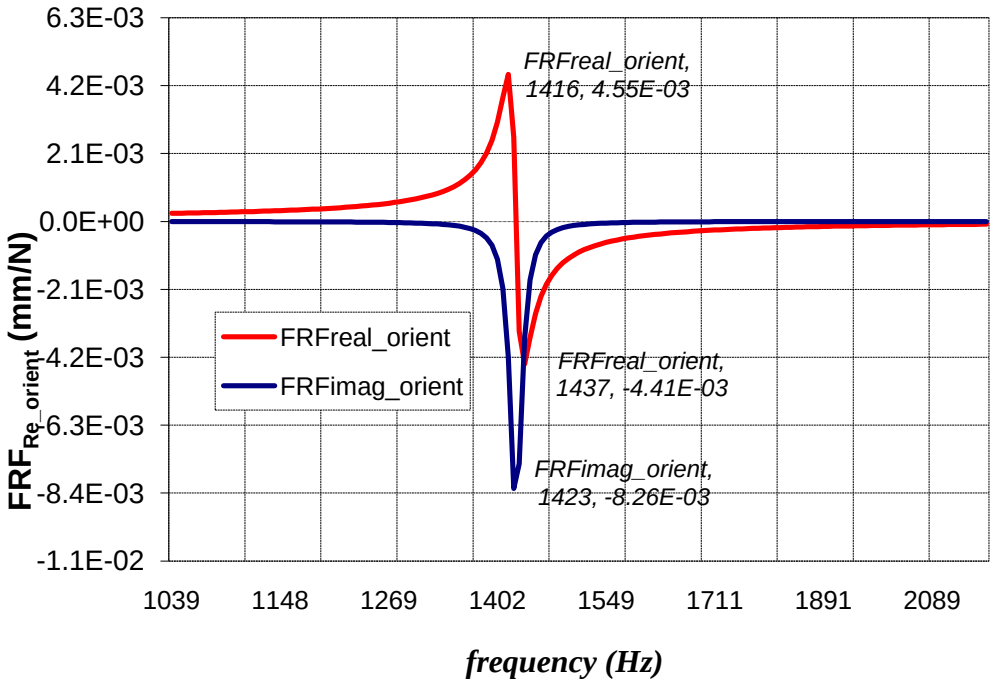

Figure 23. Real and Imaginary parts of the machining system
(Tool cutting tool geometry of helix 35 rake 18)

The peak frequencies in the reproduced SDOF equation plots were extracted to compare with the actual measurement taken. The error was found to be less than 1% as compared to the measured values as shown in Table 17.

TABLE 17

FRF DATA EXTRACTED FROM REPRODUCED PLOTS (HELIX 35/ RAKE 18)

Peak frequencies	**Actual**	**Reproduced**	**% Error**
f_1	1410	1416	0.46%
f_2	1428	1437	0.63%
f_n	1426	1423	-0.21%

Since the reproduced equation of motion plots had minimal error with the actual measurement, the SLDs were generated to enable evaluating the tool design parameters as shown in Figure 24. The minimal critical depth of cut was 0.1293 mm at any spindle speed within the capacity of the machine. It is also possible to check alternative cutting parameters that would provide maximum material removal rate.

Using the same additional input data as listed for the end mill with helix angle 35 degree and rake angle 18 degree, and the dynamic characteristics data for helix 45 and rake angle 10 degree, the reproduced real and imaginary parts were plotted in Figure 25.

The peak frequencies for the machining system with end mill helix 45 and rake 10 in the reproduced SDOF equation plots were compared with the measured values. Less than 1% error was found as compared to the measured values as shown in Table 18.

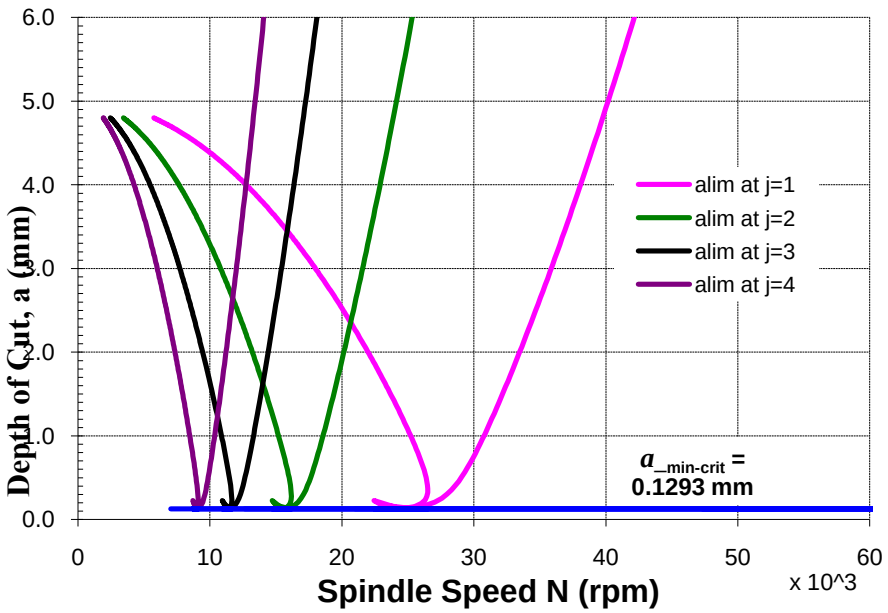

Figure 24. SLD Diagram for the machining system with cutting tool
(Helix 35 rake 18 at overhang length x = 3 inches)

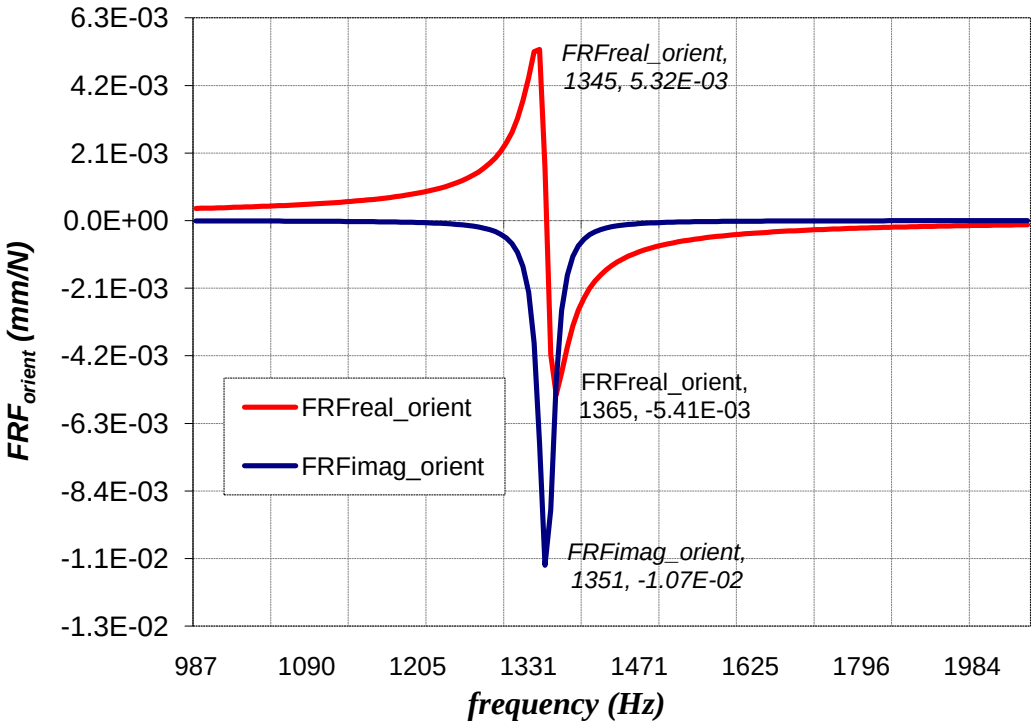

Figure 25. Real and Imaginary parts of the tool cutting tool geometry of helix 45 rake 10

TABLE 18

FRF DATA EXTRACTED FROM REPRODUCED PLOTS (HELIX 45/ RAKE 10)

Peak frequencies	Actual	Reproduced	% Error
f_1	1334	1345	0.82%
f_2	1356	1365	0.66%
f_n	1353	1351	-0.15%

After having made the SDOF plots, SLDs were created to evaluate the machining parameters for the selected tool. The parameters were evaluated in Figure 26. The minimal critical depth of cut was 0.1088 mm at any spindle speed within the capacity of the machine. Therefore, based on the SLD plots, the stability regions were determined and it would be possible to achieve maximum material removal rate through evaluation of the cutting parameters.

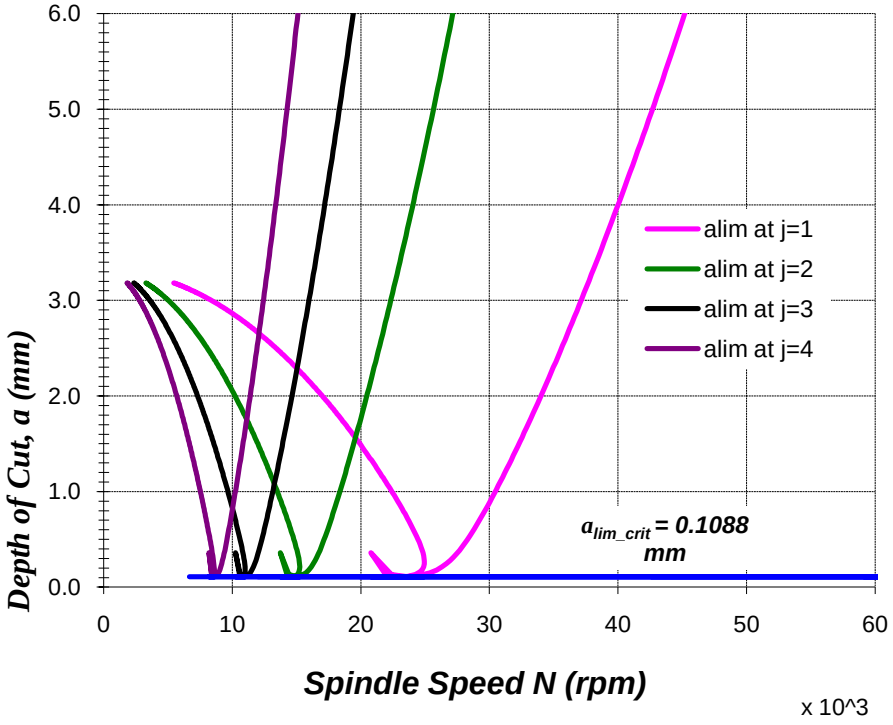

Figure 26. SLD Diagram for the machining system
(Helix 45 rake 10 at x=3.0 inch-OH length)

5.3 Methodology for Determining Cutting-Tool Design Parameters

In the third step, a methodology for determining the cutting-tool design parameters was developed to achieve desired performance levels for a given machining system. This process began by proposing design changes on the original tool design. It involved creating a CAD model and constructing the stereolithography model. Measurement were collected of the new design of the frequency response function values, f_1, f_2, and f_n, with respective peak values of real part G_{max} and G_{min}, and H or Imaginary G_{min} using the impact hammer tester. The machining system's dynamic characteristics, including the damping ratio ζ and stiffness k to create a stability lobe diagram, were then predicted. Finally, the cutting-tool design parameters, such as chatter-free depth of cut a_p and spindle speed N, were determined in order to achieve the maximum material removal rate with the desired performance target level. The procedure for evaluating the tool design parameters are shown in Figure 27. The steps are as follows:

Step 1. Propose Tool Design (CAD)

Step 2. Build the SL model for the proposed tool design.

Step 3. Impact test SL model on the machining system and analyze for systems dynamic characteristics.

Step 4. Predict the machining system dynamic characteristics with the proposed tool design.

Step 5. Generate a stability lobe diagram to evaluate the tool design and its ability to achieve maximum material removal rate (MMR).

Step 6. If the desired MMR is attained, order the tool; otherwise, redesign the tool and go back to step 2.

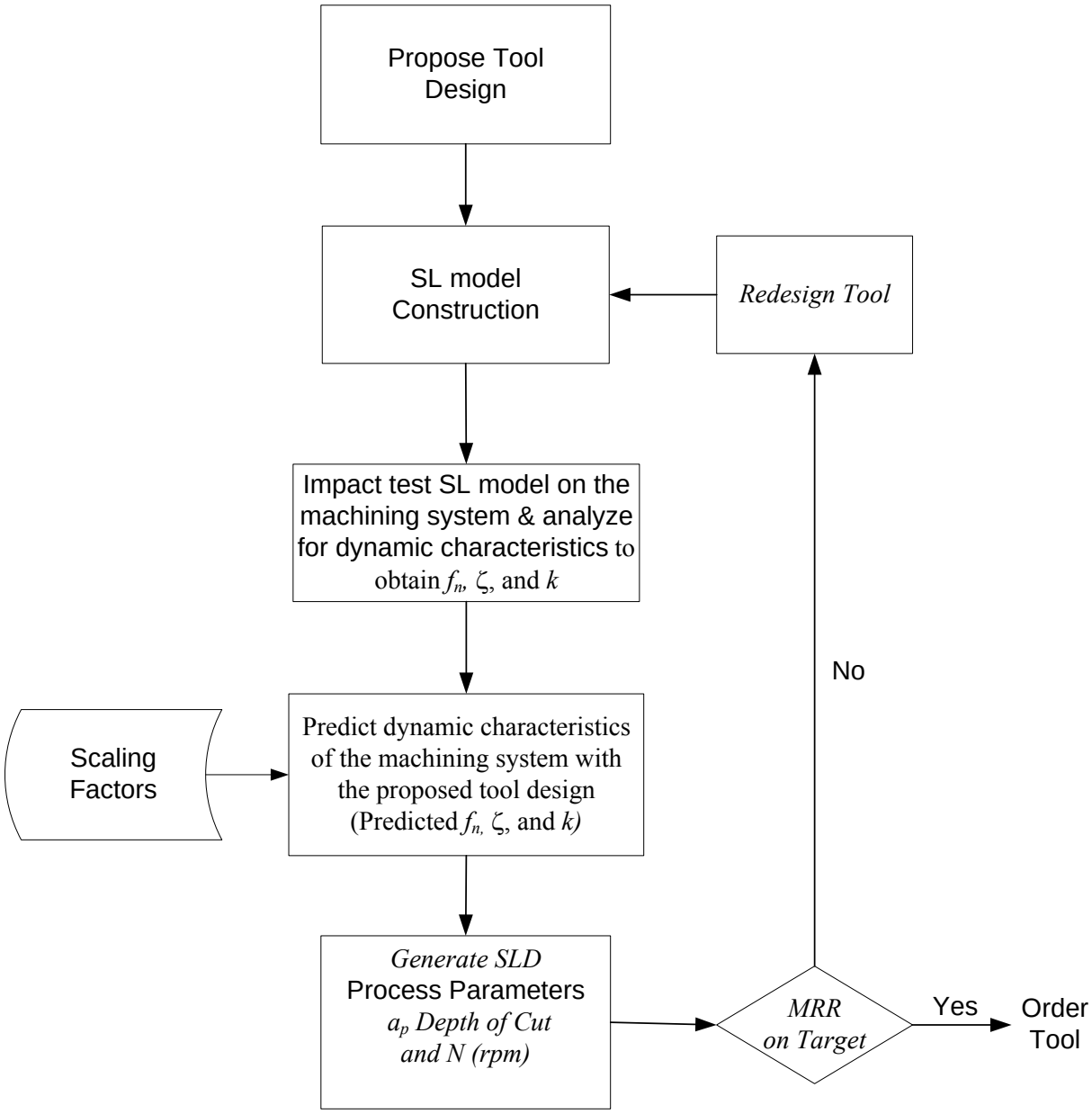

Figure 27. Procedure for evaluating tool design parameters.

Evaluation of tool design parameters and verification of results will be presented in Chapter 6. Dynamic characteristics of the new tool are predicted using the SL model of the new tool design followed by creation of SLDs to evaluate the tool design parameters.

CHAPTER 6

EVALUATION OF CUTTING DESIGN PARAMETERS

The experimental modal analysis for a machining system's dynamic characteristics such as natural frequency f_n, damping coefficient ζ, and stiffness k are determined prior to creating the stability lobe diagram. In this verification process, a new tool proposed by changing mainly the cutting-edge helix to 30 degrees and rake to 10 degrees. It was a ball-nose type end mill, diameter ¾ inch, length 5 inches, and flute length 2 inches. SL model was fabricated for this material using the SL material property described in section 4.1, Table 4.

The corresponding SL model was constructed for the proposed tool design using the construction process in Figure 11. This SL model was clamped at 3.0 inch-overhang length in the same machining system and experiment was performed using impact hammer tester. EMA was performed following FRF measurements. The resulting dynamic characteristics for the proposed tool design were then predicted using the scale factor determined for the same machining system. The prediction results were shown in Table 19.

TABLE 19

PREDICTING DYNAMIC CHARACTERISTICS
OF MACHINING SYSTEM USING SL MODEL

Helix 30, Rake 10			
Dynamic Parameter	SL Model	Scale Factor	Predicted Carbide Tool (CT)
f_1 (Hz)	710	1.94	1374
f_2 (Hz)	723	1.94	1400
f_n (Hz)	719	1.94	1392
k (N/m)	4.56E+04	63.59	2.90E+06
ζ	0.012	0.45	0.005

In this study, the SLD was created for the predicted tool and actual tool with a cutting geometry of helix angle 30 degrees and rake 10 degrees, and any discrepancies in the prediction system were investigated. Some additional input for the milling process included the following: material Al-7075-T6, cutting force angle β, and immersion entry and exit angles, ϕ_s and ϕ_e, respectively.

6.1 Verification of Results

The machining system dynamic characteristics with the actual end mill were compared with the predicted value for the same machining system. The actual tool in the machining system was impact tested and the dynamic characteristics were analyzed. Results were shown along with the predicted values on Table 20. The results indicated a maximum of 1.4% error for predicting the natural frequencies f_n, and less than 5% for predicting stiffness k of the machining system.

TABLE 20

COMPARISON OF THE PREDICTED VERSUS ACTUAL DYNAMIC CHARACTERISTICS

Helix 30, Rake 10					
Dynamic Parameter	SL Model	Scale Factor	Predicted Carbide Tool (CT)	Actual Carbide Tool (CT)	Error (%)
f_1	710	1.94	1374	1363	0.8
f_2	723	1.94	1400	1375	1.9
f_n	719	1.94	1392	1372	1.4
k	4.56E+04	63.59	2.90E+06	3.03E+06	-4.4
ζ	0.012	0.45	0.005	0.005	4.9

6.2 Generation of Stability Lobe Diagram

By using the data for the predicted and actual tool with helix 30/rake 10, shown earlier in Table 20, the real and imaginary parts of the FRF data were applied to reproduce the SDOF equation and identify the region of instability and chatter generation. Then, the stability lobe diagram was created for 3.0 inch-overhang distance.

These plots not only represent that the single degree of freedom equation was reproduced but also identify the chatter generation and the region of instability in the real-part plot. The high-chatter frequency is mostly detected between the natural frequency and the maximum frequency. Plot (a) in Figure 28 illustrates the real part of the FRF, and plot (b) illustrates the imaginary part of the FRF. For comparison, the actual and predicted end mill are labeled in plots (a) and (b), and the error, found to be less than 2% for 3.0 inch-overhang length as shown in Table 21.

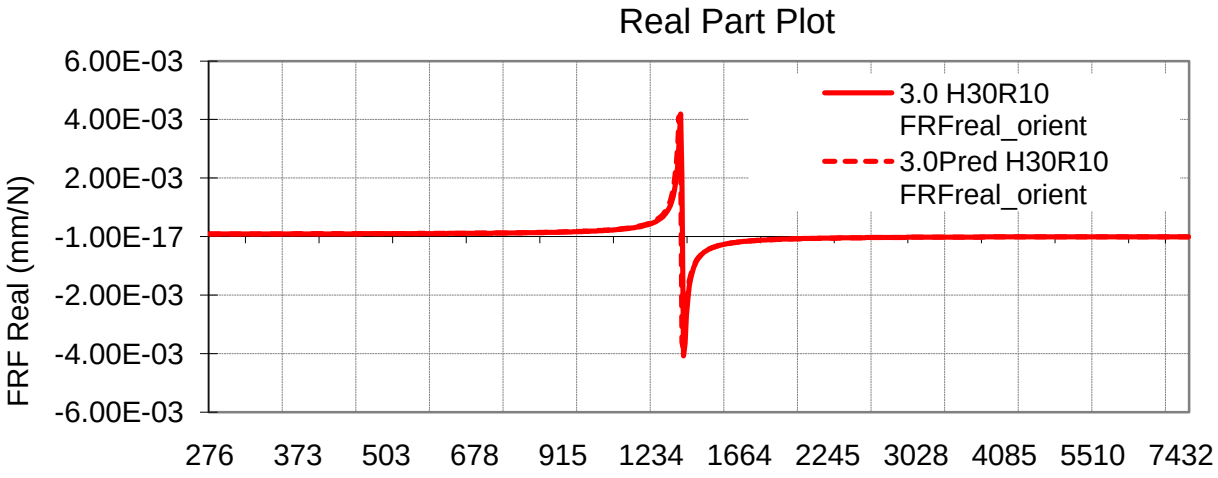

(a)

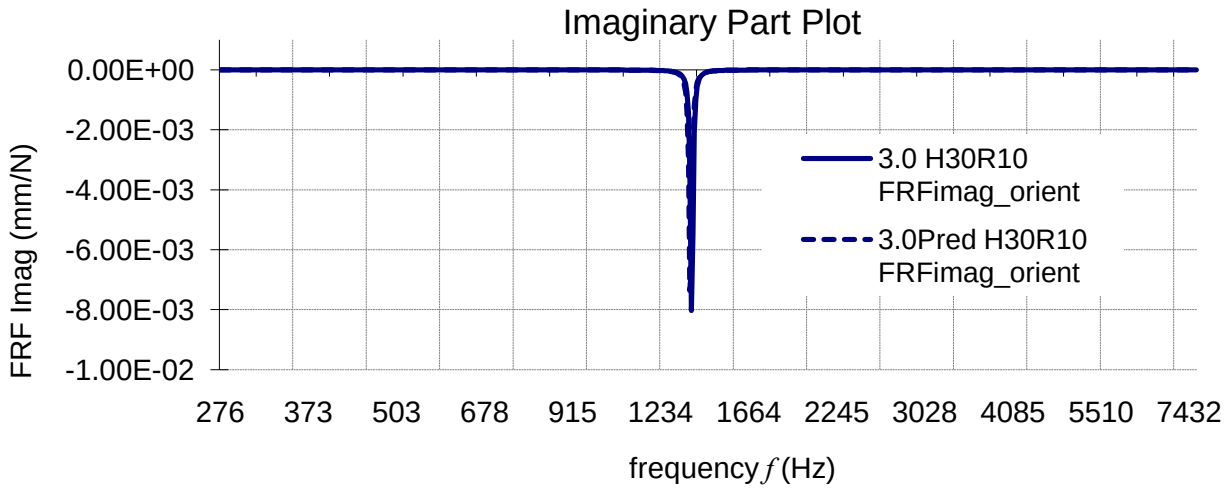

(b)

Figure 28. Actual and predicted end mills: (a) real part and (b) imaginary part of FRF measured at *x* 3.0 inch-overhang length.

TABLE 21

FRF DATA AS EXTRACTED FROM REPRODUCED INITIAL SDOF CHARTS (PREDICTED VERSUS ACTUAL COMPARISON)

End Mill Helix 30/Rake 10	**Peak Frequency**	**Predicted End Mill**	**Actual End Mill**	**Percent Error**
3.0-Inch Overhang	f_1	1,381	1,363	1.32
	f_2	1,402	1,377	1.83
	f_n	1,388	1,370	1.31

Furthermore, the stability lobe diagrams, shown in Figure 29, were generated to evaluate the tool design parameters such as axial depth of cut and spindle speed. The minimum critical axial depths of cut for the predicted and actual machining system with the proposed tool are obtained on the SLD. The minimum critical cutting depth $a_{min\text{-}critical}$ for the predicted cutting tool was 0.1434 mm, and the actual cutting tool was 0.1404 mm for any spindle speed *N* within the

capacity of the machining system. There was a 2.1% error observed when the predicted versus actual critical depth of cuts were compared. This value shown can be run at any spindle speed within the available capacity range of the machine. Design alternatives can be evaluated to achieve the maximum material removal rate with the most economic condition.

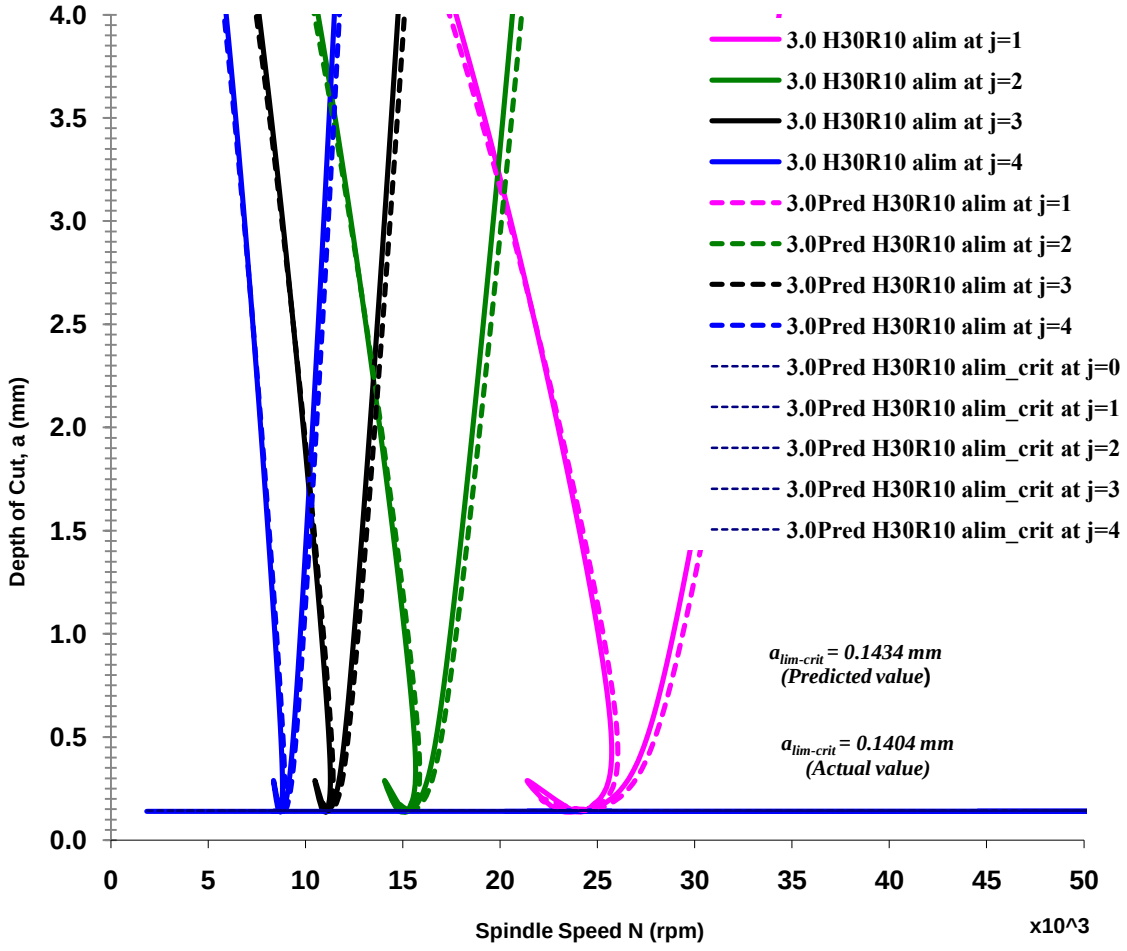

Figure 29. SLD plot for actual and predicted machining systems at 3.0 inch-OH with cutting tool geometry helix 30/rake 10.

In summary, it is possible to translate the experimental modal analysis results into a stability lobe diagram and evaluate the tool design parameters. Results indicated the value of utilizing the SL model in evaluating the tool design before actually producing or ordering it. The SL model for the end mill with helix 30/rake 10, was used to validate the procedure and methodology to determine the tool design parameters. Further elaboration of the reproduction techniques of SDOF plots and SLDs are presented in Appendices A and B.

6.3 Material Removal Rate Calculations

Now the predicted cutting tool geometry of a solid carbide tool with helix 30/rake 10 are considered in order to determine the chatter-free zone and calculate the MRR, where $MRR = ahs = ahs_z zN$. The input data per SLD, as shown in Figure 30, would be as follows:

Selected Parameter

Material → Al-7075-T6, k_s = 800 N/m^2

Spindle speed N_1 = 45,000 rpm

Cutting depth a = 0.138 mm

Chip thickness (assume) = 0.05 mm

Feed per teeth s_z = 0.02 mm

Number of teeth z = 2

MRR = 12.42 mm^3/min

Optional Parameter

Same material

Spindle speed N_2 = 21,000 rpm

Cutting depth a = 2.2 mm

Chip thickness (assume) = 0.05 mm

Feed per teeth s_z = 0.02 mm

Number of teeth z = 2

MRR = 92.4 mm^3/min

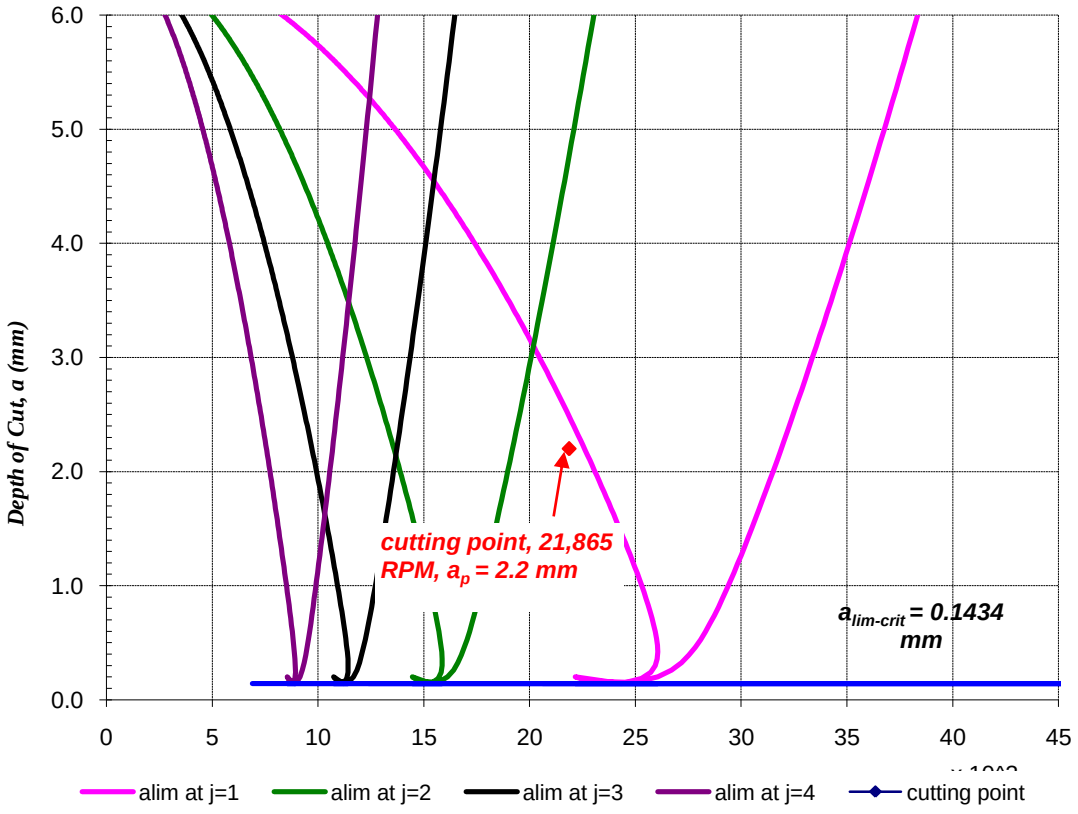

Figure 30. Example of stability lobe diagram of solid carbide end mill with cutting geometry helix 30/rake 10.

The parameters taken from the SLD shown in Figure 30 indicate that there were multiple options for improving the MRR using the SLD stable regions. Therefore, there were ample opportunities that not only higher MRR though creation of SLD could be achieved, but also that self-excited chatter could be prevented by distinguishing between the stable and unstable regions indicated in the SLD. Hence, the combination of predicting dynamic characteristics using SL models and SLD generation to evaluate the cutting tool design parameters would greatly enhance the advancement of HSM technology.

CHAPTER 7

CONCLUSIONS AND FUTURE RESEARCH

The main focus of this research was to demonstrate the value of using stereolithography models in predicting the dynamic characteristics of machining systems and to develop a methodology for evaluating proposed tool designs proactively.

In this research, the value of using stereolithography models in predicting the dynamic characteristics of a given machining system was demonstrated. An initial investigation was performed using solid bars of a carbide tool and SL models employing free-free boundary excitation. The natural frequencies were measured through vibration testing using the popular method of excitation, i.e., an impact hammer. The results from this experimental method were compared with the Bernoulli-Euler analytical method and the finite element method. This study indicated that the FEM result deviated 1.6% from that of the actual carbide barstock. On the other hand, results obtained using SL models deviated 2% from that obtained using the FEM and 3.7% of that calculated using the Bernoulli-Euler method.

Another study, using the same experimental setup, was performed to investigate the relationship between the measured values of the natural frequencies of actual carbide end mills and their SL models. Findings indicated that changes in the end-mill geometry resulted in variations in the natural frequencies while the scaling factor for different geometries remained the same. This is in agreement with the results reported by Dornfeld (1995). These results were considered acceptable and indicated that SL models are of use in predicting the dynamic characteristics of actual cutting tools.

Based on the above, further investigations of the effect of changes in the boundary conditions were performed. This study involved an actual machining system on which samples

of carbide barstock and their SL models were clamped a distance *x* from their ends. The resulting natural frequency and stiffness of both samples demonstrated a decreasing trend with an increase in the distance *x*.

Studies involving an actual milling machine with selected end mills and their SL models were conducted to determine values of the scaling factor that can be used to predict the dynamic characteristics of the machining system. Such dynamic characteristics included the natural frequency, stiffness, and damping coefficient. These values are required for generating stability lobe diagrams and determining critical values of the spindle speed and depth of cut.

This procedure was validated using a new geometry of the end mill on the same milling machine. The resulting stability lobe diagram correlated well with that of the actual carbide end mill. This represents a proactive approach to evaluating tool designs and overcoming limitations in cited analytical and numerical methods.

In conclusion, practitioners can generate stability lobe diagrams and study tool design alternatives before producing or ordering a required tool using stereolithography models. The proposed method helps overcome limitations in cited analytical and numerical methods since no simplifying assumptions are needed. The predicted values are of machine specific and help customize tool design.

The procedure developed in this research indicated that SL models can be used to predict high-speed milling dynamics. While the procedure was applied for evaluating different designs of carbide end mills, used essentially on the same milling machine, the same procedure could have been used to evaluate different tool materials and cutting tools. This represents a natural extension of this research. In addition, future research may address one or more of the following areas:

1) Effect of changes in the SL resin

This research considered the one resin available at the rapid prototyping laboratory: 11120 WaterShed™. However, other resin types can be used to develop SL models. Research efforts may involve understanding the effect of changing SL resins on values of the scaling factor. It would be useful to create calibration charts to help tool practitioners' select appropriate scaling factors for specified combinations of tool and model materials.

2) Evaluation of coated tools

In some applications, coated solid end mills are used to improve the performance of the cutting tool. Research in this area would consider methods by which SL models can be adjusted to reflect the effect of coating. These may include efforts to apply similar coats to the SL models or adjust the dimensions of the tool model.

3) Workpiece-fixture subsystem

This research could be extended to studying the dynamic characteristics of other components of the machine tool system such as the workpiece-fixture subsystem. This research would allow evaluation of fixture design and its ability to withstand the cutting forces, and achieve stiffness and rigidity requirements.

BIBLIOGRAPHY

BIBLIOGRAPHY

Altintas, Y., 2000, *Manufacturing Automation*, Cambridge University Press.

Altintas, Y., 2001, "Analytical Prediction of Three Dimensional Chatter Stability in Milling," *JSME, International Journal Series C, Mechanical Systems, Machine Elements and Manufacturing*, V44 (3), pp. 717–723.

Altintas, Y., and Budak, E., 1995, "Analytical Prediction of Stability Lobes in Milling," *Annals of the CIRP*, V44 (1), 357–362.

Altintas, Y., and Budak, E., 1998, "Analytical Prediction of Chatter Stability Conditions for Multi-Degree of Systems in Milling," Part I. Modeling; Part II. Applications, *Transactions of ASME, Journal of Dynamic Systems, Measurement and Control*, 120, pp. 22–36.

Altintas, Y., and Chan, P., 1992, "In-Process Detection and Suppression of Chatter in Milling," *International Journal of Machine Tools Design and Research*, V32 (3), pp. 329–347.

Altintas, Y., Shamoto, E., Lee, P., and Budak, E., 1999, "Analytical Prediction of Stability Lobes in Ball-End-Milling," *Transactions of ASME, Journal of Manufacturing Science and Engineering*, V121, pp. 586–592.

Arnold, R. N., 1946, "The Mechanism of Tool Vibration in the Cutting of Steel," *Proceedings of Institution of Mechanical Engineers*, V154 (4), pp. 261–284.

Automotive Industry Action Group (AIAG), 1994. *Measurement Systems Analysis Reference Manual*, Chrysler, Ford, General Motors Supplier Quality Requirements Task Force.

Automotive Industry Action Group (AIAG), 2002. *Measurement Systems Analysis Reference Manual,* 3rd edition, Chrysler, Ford, General Motors Supplier Quality Requirements Task Force.

Budak, E., 2006a, "Analytical Methods for High Performance Milling," Part I. Forces, Form Error and Tolerance Integrity, *International Journal of Machine Tools and Manufacture*, V46, pp. 1478–1488.

Budak, E., 2006b, "Analytical Models for High Performance Milling" Part II. Process Dynamics and Stability, *International Journal of Machine Tools & Manufacture*, V46, pp. 1489–1499.

Chockalingam, K., Jawahar, N., and Chandrasekhar, U., 2006, "Influence of Layer Thickness on Mechanical Properties in Stereolithography," *Rapid Prototyping Journal*, V12 (2), pp. 106–113.

Craig, R., and Kurdila A., 2006, *Fundamentals of Structural Dynamics*, 2nd Edition, John Wiley & Sons, Inc., Hoboken, New Jersey.

BIBLIOGRAPHY (continued)

Dalton, H., Byrne, G., and Steinicke, M., 2008, "Evaluation of a Model for the Prediction of Milling Stability for Thin-Walled Components," *International Journal of Manufacturing Technology and Management*, V15 (2), pp. 187–196.

DeGarmo, E. P., Black, J. T., and Kohser, R. A., 2003, *Materials and Processes in Manufacturing*, 9th ed., John Wiley & Sons, Inc., New York.

Dornfeld, W., 1995, "Direct Dynamic Testing of Scaled Stereolithographic Models," *Journal of Sound and Vibration*, V29, pp. 12–17.

Dulieu-Barton, J. M. and Fulton, M. C., 2000, "Mechanical Properties of a Typical Stereolithography Resin," *Strain*, V36 (2), pp. 81–87.

Erdel, B. P., 2003, *High-Speed Machining*, Society of Manufacturing Engineers, Dearborn, Michigan.

Faassen, R. P. H., 2007, "Chatter Prediction and Control for High-Speed Milling: Modeling and Experiments," Ph.D. Dissertation, University Press, Eindhoven, The Netherlands.

Faassen, R. P. H., Van De Wouw, N., Oosterling, J. A. J., and Nijmeijer, H., 2003, "Prediction of Regenerative Chatter by Modeling and Analysis of High Speed Milling," *International Journal of Machine Tools and Manufacture*, V43, pp. 1437–1446.

Hague, R., Mansour, S., Saleh, N., and Harris, R., 2004, "Materials Analysis of Stereolithography Resins for Use in Rapid Manufacturing," *Journal of Material Science*, V39, pp. 2457–2464.

Hoshi, T., Sakisaka, N., Moriyama, I., and Sato, M., 1977, "Study for Practical Application of Fluctuating Speed Cutting for Regenerative Chatter Control," *Annals of the CIRP*, V26, pp. 175–180.

Koenigsberger, F., and Tlusty, J., 1967, *Machine Tool Structures - Vol. 1: Stability Against Chatter*, Pergamon Press.

Leigh, E. P., Schueller, J. K., Tlusty, J., and Smith, S., 2000, "Advanced Machining Techniques on Titanium Rotor Parts," American Helicopter Society 56th Annual Forum, Virginia Beach, VA.

Little, R. J. A. and Rubin, D. B., 1987, *Statistical Analysis with Missing Data*, John Wiley & Sons, Inc., New York.

Liu, B., Gong, X., and Chappell, W. J., 2004). "Applications of Layer-By-Layer Polymer Stereolithography for Three-Dimensional High-Frequency Components," *IEEE Transactions on Microwave Theory and Techniques*, V52 (11), pp. 2567–75.

Mahn, J., and Bayly, P., 1998, "Impact Testing of Stereolithographic Models to Predict Natural Frequencies," *Journal of Sound and Vibration*, V224 (3), pp. 411–430.

Mansour, S., Gilbert, M., and Hague, R., 2007, "A Study of the Impact of Short-Term Aging on the Mechanical Properties of a Stereolithography Resin," *Journal of Material Science and Engineering A*, V447 (1–2), pp.277–284.

Manufacturing Laboratories, Inc., http.//www.mfg-labs.com/4/17/2009.

Merritt, H. E., 1965, "Theory of Self-Excited Machine Tool Chatter," *Journal of Engineering for Industry*, V87 (4), pp. 447–454.

Montgomery, Douglas C., and Runger, George C., 1993–94a, "Gauge Capability and Designed Experiments". Part I. Basic Methods, *Quality Engineering*, V6 (1), pp. 115–135.

Montgomery, Douglas C., and Runger, George C., 1993–94b, "Gauge Capability Analysis and Designed Experiments". Part II. Experimental Design Models and Variance Component Estimation, *Quality Engineering*, V6 (2), pp. 289–305.

Noorani, R., 2005, *Rapid Prototyping Principles and Applications*, John Wiley & Sons, Inc., Hoboken, New Jersey.

Nwokah, Osita D. I., and Hurmuzlu, Y., 2001, "Machine Tool Dynamics and Vibrations," Chapter 4, in *The Mechanical Systems Design Handbook*, CRC Press.

Opitz, H., and Bernardi, F., 1970, "Investigation and Calculation of the Chatter Behavior of Lathes and Milling Machines," *Annals of the CIRP*, V18 (1), pp. 335–343.

Schmitz, T. L., and Donaldson, R. R., 2000, "Predicting High-Speed Machining Dynamics by Substructure Analysis," *Annals of the CIRP*, V49 (1), pp. 303–308.

Schmitz, T. L. and Smith, K. S., 2008, *Machining Dynamics: Frequency Response to Improved Productivity*, Springer.

Searle, S. R., Casella, G., and McCulloch, C. E., 1992, *Variance Components*, John Wiley & Sons, Inc., New York.

Shaw, M. C., 2005, *Metal Cutting Principles*, 2nd Edition, Oxford University Press, New York.

Smith, S., and Tlusty, J., 1990, "Update on High Speed Milling Dynamics," *Journal of Engineering for Industry*, V112, pp. 142–149.

Smith, S., and Tlusty, J., 1991, "An Overview of Modeling and Simulation of the Milling Process," *Journal of Engineering for Industry*, V113, pp. 169–175.

Sridhar, R., Hohn, R. E., and Long, G. W., 1968a, "A Stability Algorithm for the General Milling Process," *Transactions of ASME, Journal of Engineering for Industry*, V90, pp. 330–334.

Sridhar, R., Hohn, R. E. and Long, G. W., 1968b, "General Formulation of the Milling Process Equation," *Transactions of ASME, Journal of Engineering for Industry*, V90, pp. 317–324.

Stépán, G., 1989, *Retarded Dynamical Systems. Stability and Characteristic Functions*, Longman, London.

Stépán, G., 1998, *Delay-Differential Equation Models for Machine Tool Chatter, in Nonlinear Dynamics of Material Processing and Manufacturing* (Ed. F. C. Moon), John Wiley & Sons, Inc., New York, pp. 165–192.

Stépán, G., 2001, "Modeling Nonlinear Regenerative Effects in Metal Cutting," *Philosophical Transactions of the Royal Society*, London, V359 (A), pp. 739–757.

Stephenson, D. and Agapiou, J., 2006, *Metal Cutting Theory and Practice*, Boca Raton: RC Press.

Taylor, F. W., 1907, "On the Art of Cutting Metals," *ASME Transactions*, V28, pp. 31–350.

Tekeli, A., and Budak, E., 2005, "Maximization of Chatter-Free Material Removal Rate in End Milling Using Analytical Methods," *Machining Science & Technology*, V9 (2), pp. 147–167.

Thomson, W.T., 1993, *Theory of Vibration with Applications*, Prentice Hall, London.

Tlusty, J., 1965, *Machine Dynamics, Handbook of High Speed Machining Technology*, King, R. I., ed., Chapman and Hall, New York, Ch. 3, pp. 8–153.

Tlusty, J., 1986, "Dynamics of High-Speed Milling," *Journal of Engineering for Industry, Trans. ASME*, 108, pp. 59–67.

Tlusty, J., 2000, *Manufacturing Processes and Equipment*, Prentice Hall, New Jersey.

Tlusty, J., Zaton, W., and Ismail, F., 1983, "Stability Lobes in Milling," *Annals of the CIRP*, V32 (1), pp. 309–313.

Tlusty, J., Ziegert, J., and Ridgeway, S., 1999, "Stiffness of Structures and Drives in Fast Milling Machines," *SAE Technical Paper Series 1999-01-2273*.

Tobias, S. A., 1965, *Machine Tool Vibration*, John Wiley & Sons, Inc., New York.

Usher, J., Roy, U., and Parsaei, H., 1998, *Integrated Product and Process Development: Methods, Tools, and Technologies*, John Wiley & Sons, Inc., New York.

Weheba, G. and Sanchez-Mersa, A., 2006, "Using Response Surface Methodology to Optimize the Stereolithography Process," *Rapid Prototyping Journal*, V12 (2), pp. 72–77.

APPENDICES

APPENDIX A

CREATION OF STABILITY LOBE DIAGRAMS

This comparison exercise uses three geometries: helix 45/rake 10, helix 35/rake 18, and helix 30/rake 10. In chapter 6, analysis of the SLD for helix 30/rake 10 plots were produced; however, the SLD analyses for helix 45/rake 10 and helix 35/rake 18 were not generated at 2.5 and 3.5 inch-OH lengths. To create their SLDs, the dynamic characteristics results are shown in Table A-1. According to the steps used to generate the SLD, reproduction of the SDOF plots of the real and imaginary parts of the FRF took place first, followed by the SLD.

The real and imaginary plots for the cutting tool geometry with helix 45/rake 10 of the reproduced SDOF are shown in Figure A-1 for overhang lengths of 2.5 inches (a) and 3.5 inches (b). Their peak frequency values are also indicated on the generated SDOF plots.

The resulting SLDs for each of the reproduced plots are shown in Figure A-2 (a) and (b) for overhang lengths of 2.5 and 3.5 inches, respectively. The limiting critical cutting depth is identified for each of the overhang lengths. The minimum critical depth for overhang of 2.5 and 3.5 inches are 0.098 and 0.124 mm, respectively.

Next, the real and imaginary plots for the cutting tool geometry with helix 35/rake 18 of the reproduced SDOF are shown in Figure A-3 for overhang lengths of 2.5 inches (a) and 3.5 inches (b). Their peak frequency values are indicated on the generated SDOF plots.

TABLE A-1

DYNAMIC CHARACTERISTICS OF END MILLS AT X = 2.5, 3.0, AND 3.5 INCH-OVERHANG LENGTHS

Geometry			Helix 35, Rake 18			Helix 45, Rake 10			between % Error	
overhang Length	Dynamic Parameter	Scale Factor	Carbide Tool (CT)	SL Model (SL)	Scale (CT/SL)	Carbide Tool (CT)	SL Model (SL)	Scale (CT/SL)	Helix 35, Rake 18	Helix 45, Rake 10
2.5	f1	2.03	1765	907	1.95	1739	810	2.15	-4.0	5.8
	f2	2.03	1782	930	1.92	1755	829	2.12	-5.6	4.3
	fn	2.03	1776	919	1.93	1749	820	2.13	-4.8	5.1
	k	64.64	3.78E+06	5.76E+04	65.58159722	2.39E+06	3.75E+04	63.73	1.5	-1.4
	ζ	0.41	0.005	0.013	0.38	0.0045	0.012	0.39	-2.4	-4.6
3.5	f1	1.85	1039	584	1.78	997	535	1.86	-3.8	0.9
	f2	1.85	1080	601	1.80	1041	550	1.89	-2.7	2.5
	fn	1.85	1078	593	1.82	1041	543	1.92	-1.6	3.8
	k	63.39	1.16E+06	1.80E+04	64.25	6.62E+05	1.06E+04	62.45	1.4	-1.5
	ζ	1.29	0.020	0.014	1.43	0.021	0.016	1.31	3.3	1.7

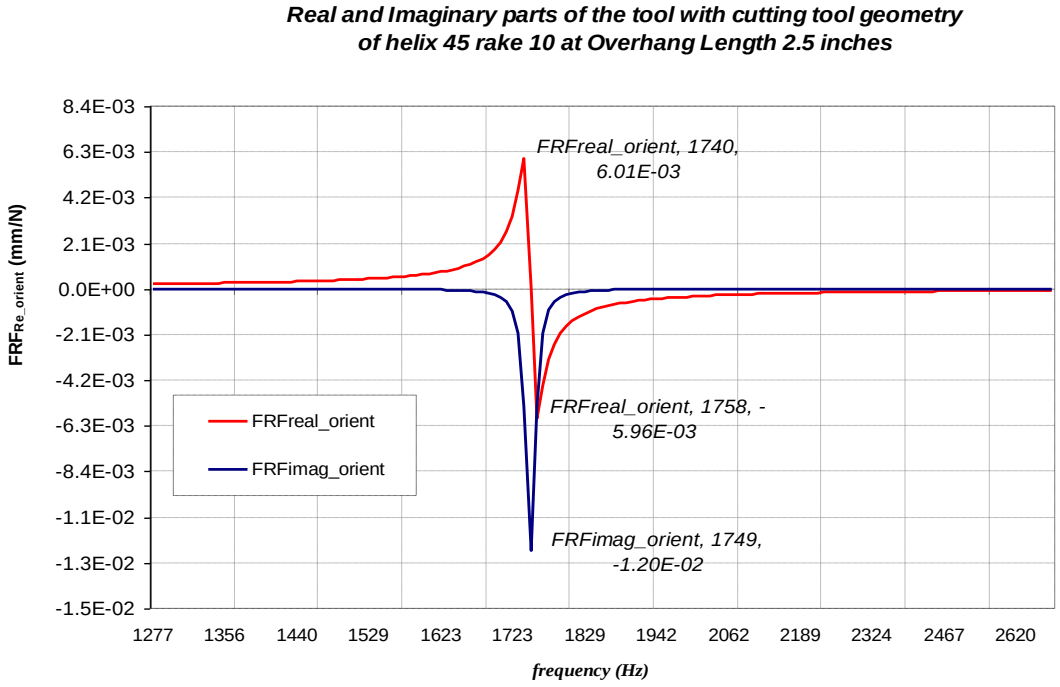

(a)

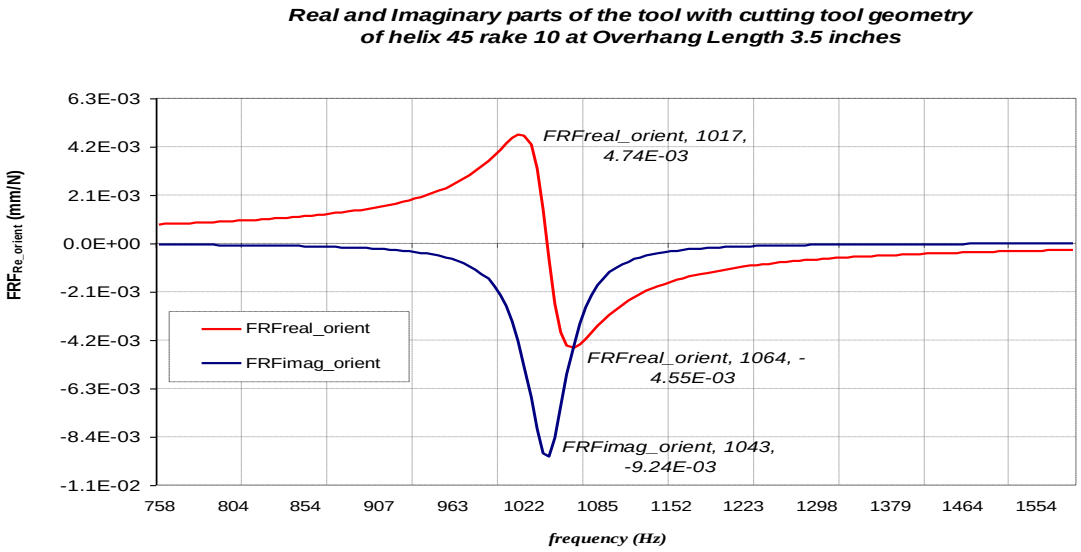

(b)

Figure A-1. Real and imaginary parts of FRF measured at overhang lengths of 2.5 inches (a), 3.0 inches (b), and 3.5 inches (c) with cutting geometry helix 45/rake 10.

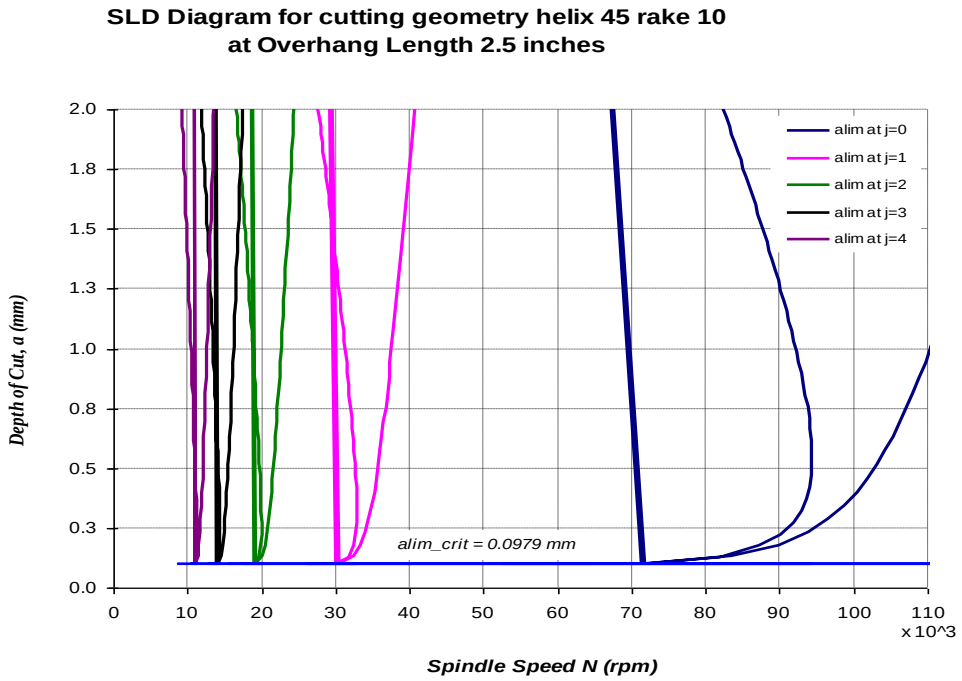

(a)

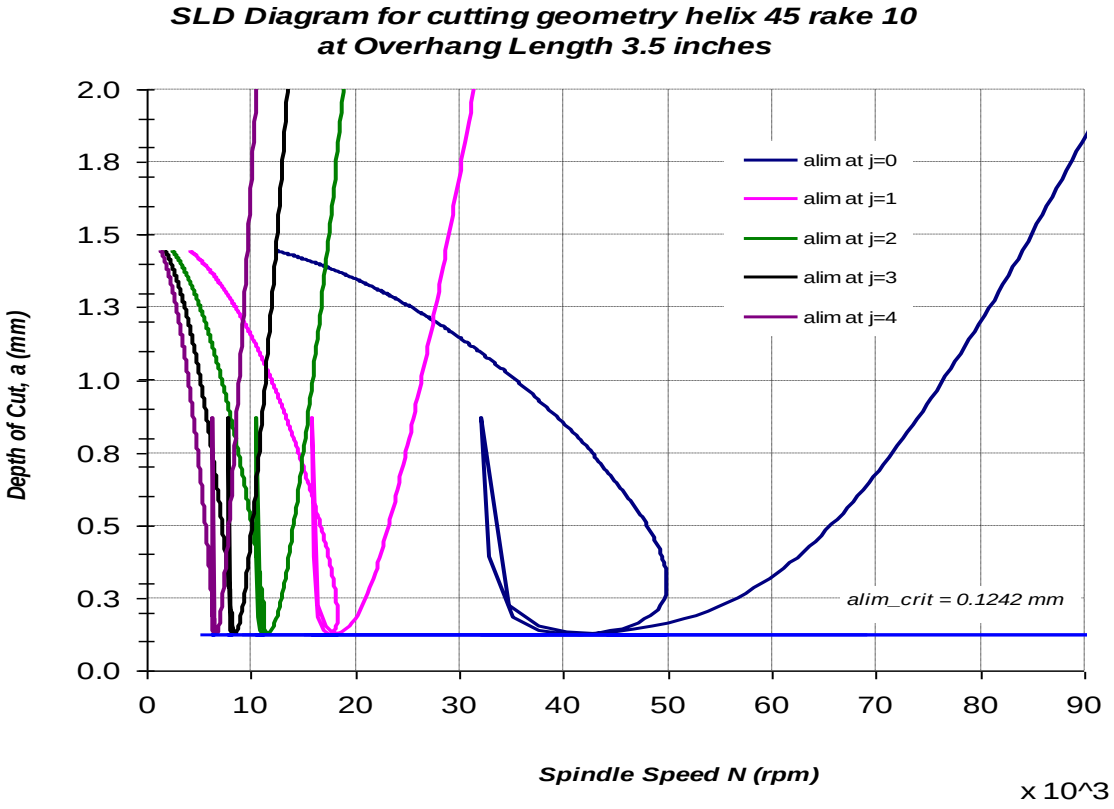

(b)

Figure A-2. SLD plots for actual machining system at overhang lengths of 2.5 inches (a), 3.0 inches (b), and 3.5 inches(c) with cutting geometry helix 45/rake 10.

As shown in Figure A-3, the peak frequencies are indicated on the reproduced SDOF plots for the three overhang lengths used in this experiment. The data shown in Table A-2 is taken from all plots and calculated for the error percentage. The error between natural frequencies is less than 0.5% and can be considered negligible. The SLDs for the tool with cutting geometry helix 35/ rake 18 at 2.5 and 3.5 inche-overhang lengths are shown in Figure A-4.

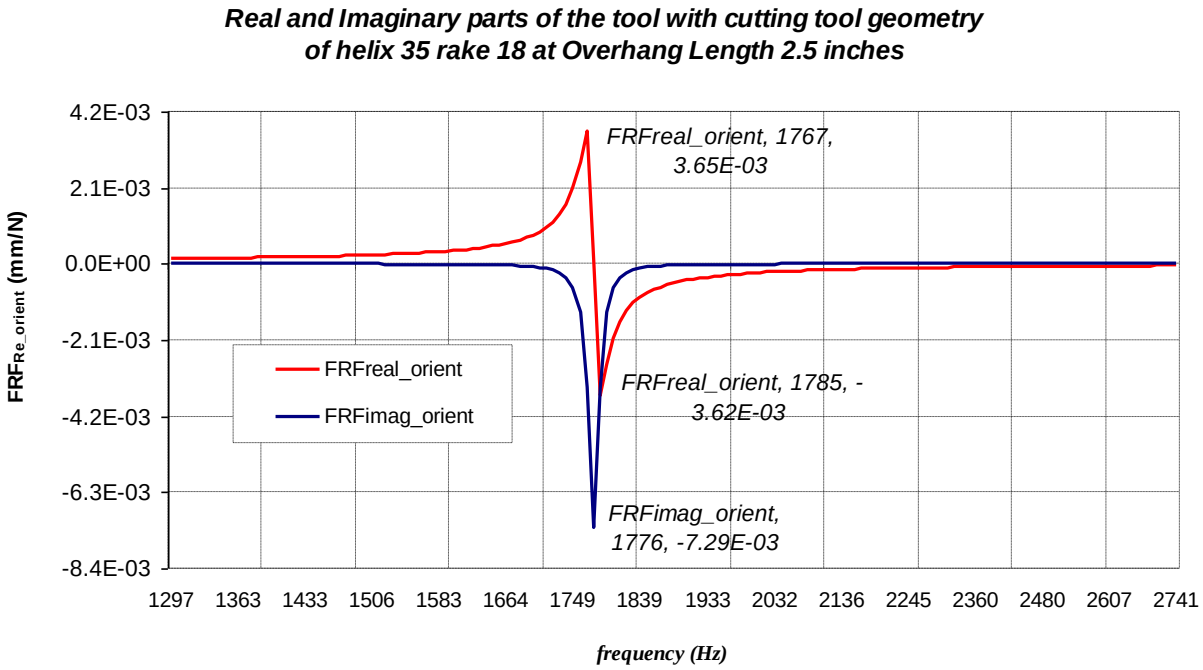

(a)

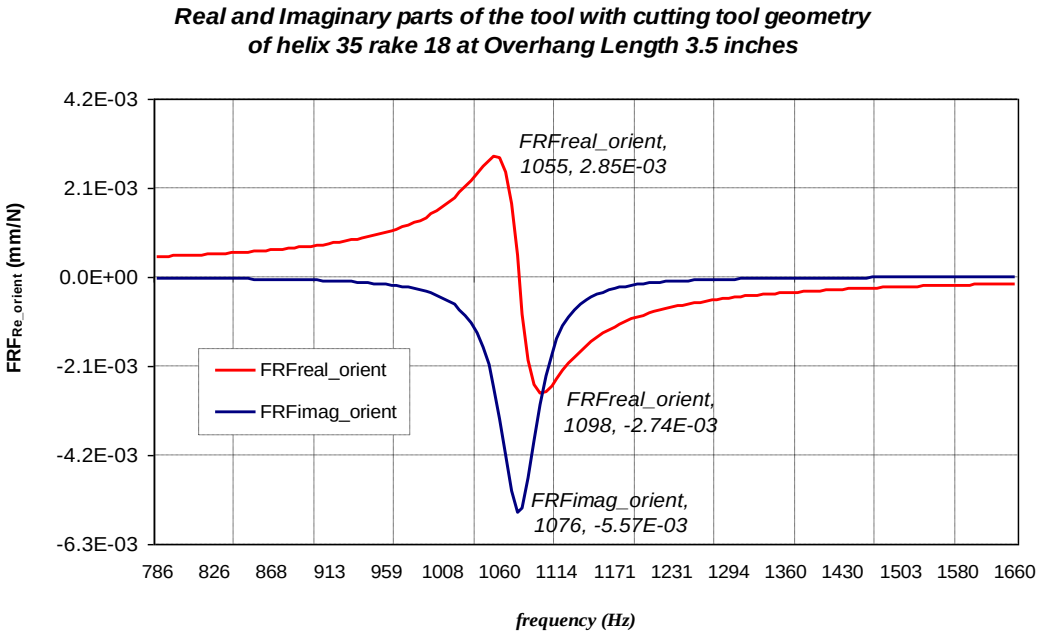

(b)

Figure A-3. Real and imaginary parts of FRF measured at overhang lengths of 2.5 inches (a) and 3.5 inches (b) for cutting geometry helix 35, rake 18.

APPENDIX A (continued)

TABLE A-2

PEAK FREQUENCIES OF REPRODUCED SDOF PLOTS
OF THREE CUTTING GEOMETRIES

Overhang Length (in)	Frequency, *f* (Hz)	H45/R10	H35/R18	H30/R10	% Error H35/R18	% Error H45/R10	% Error H30/R10
2.5	f_1	1,740	1,767	1,704	0.10	0.04	-0.12
	f_2	1,758	1,785	1,721	0.17	0.17	0.13
	f_n	1,749	1,776	1,713	0.00	0.00	-0.02
3.5	f_1	1,017	1,055	1,058	1.57	1.98	0.95
	f_2	1,064	1,098	1,090	1.70	2.21	1.11
	f_n	1,043	1,076	1,074	-0.17	0.19	-0.09

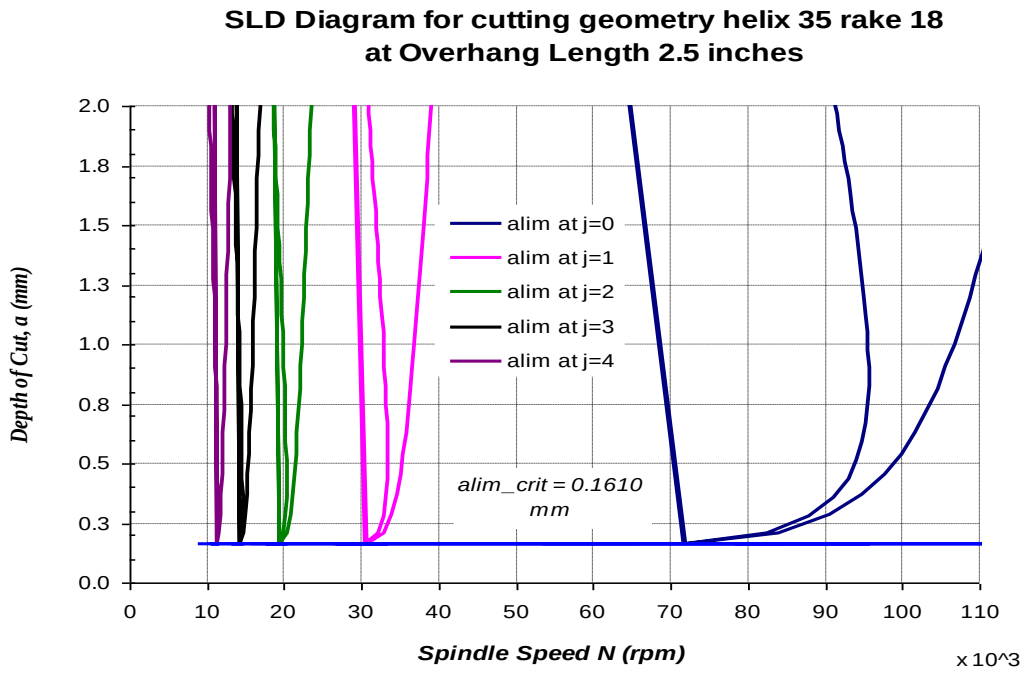

(a)

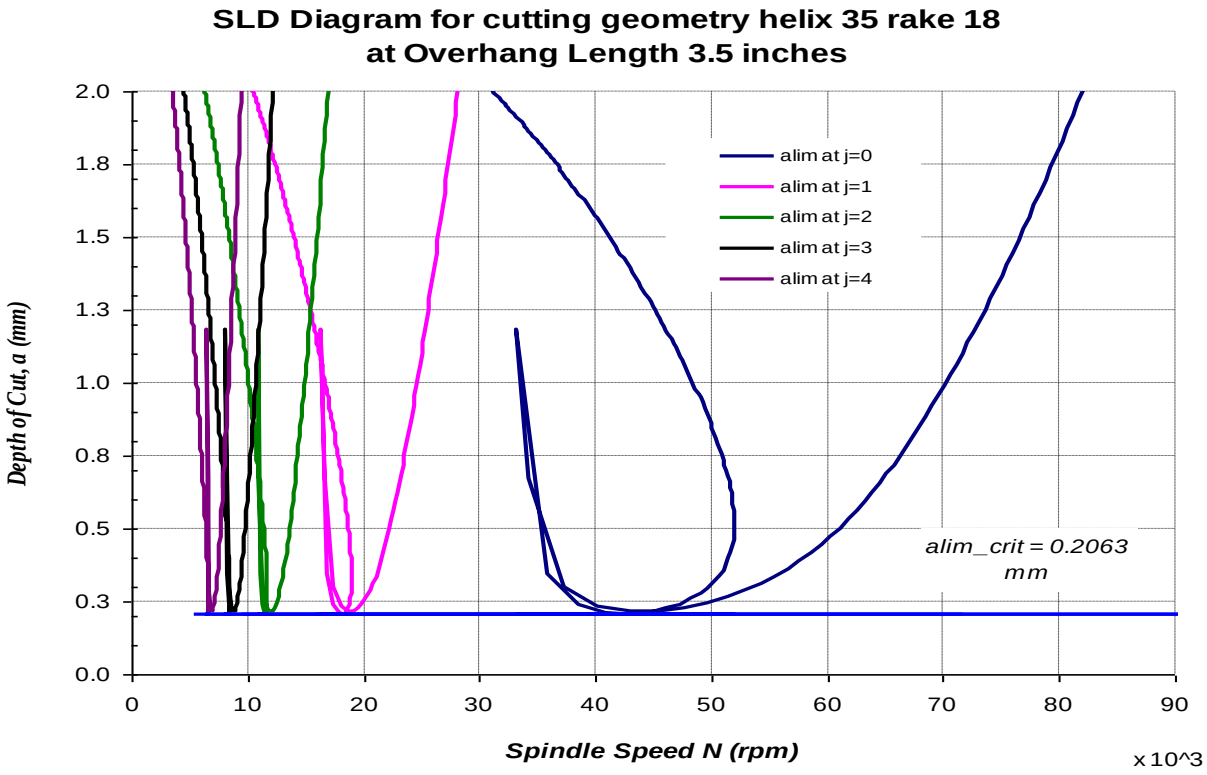

(b)

Figure A-4. SLD plots for actual machining system for overhang lengths of 2.5 inches(a), 3.0 inches (b), and 3.5 inches(c), for cutting geometry helix 35/rake 18.

The resulting SLDs of the cutting geometry helix 35/ rake 18, as shown in Figure A-4 (a) and (b) for overhang lengths of 2.5 and 3.5 inches, respectively, indicate that the chatter-free boundaries are similar to other geometries. The limiting critical cutting depths are identified for 2.5 and 3.5 inches overhang lengths and are 0.161 and 0.206 mm, respectively.

APPENDIX B

SLD COMPARISON AMONG DIFFERENT CUTTING GEOMETRIES

The appearance of three cutting geometries is shown in Figures B-1 to B-4. Figures B-1 and B-3 compare the real and imaginary parts of the three geometries. Again, a comparison of SLDs indicating the critical cutting depths and spindle speeds are shown in Figures B-2 and B-4

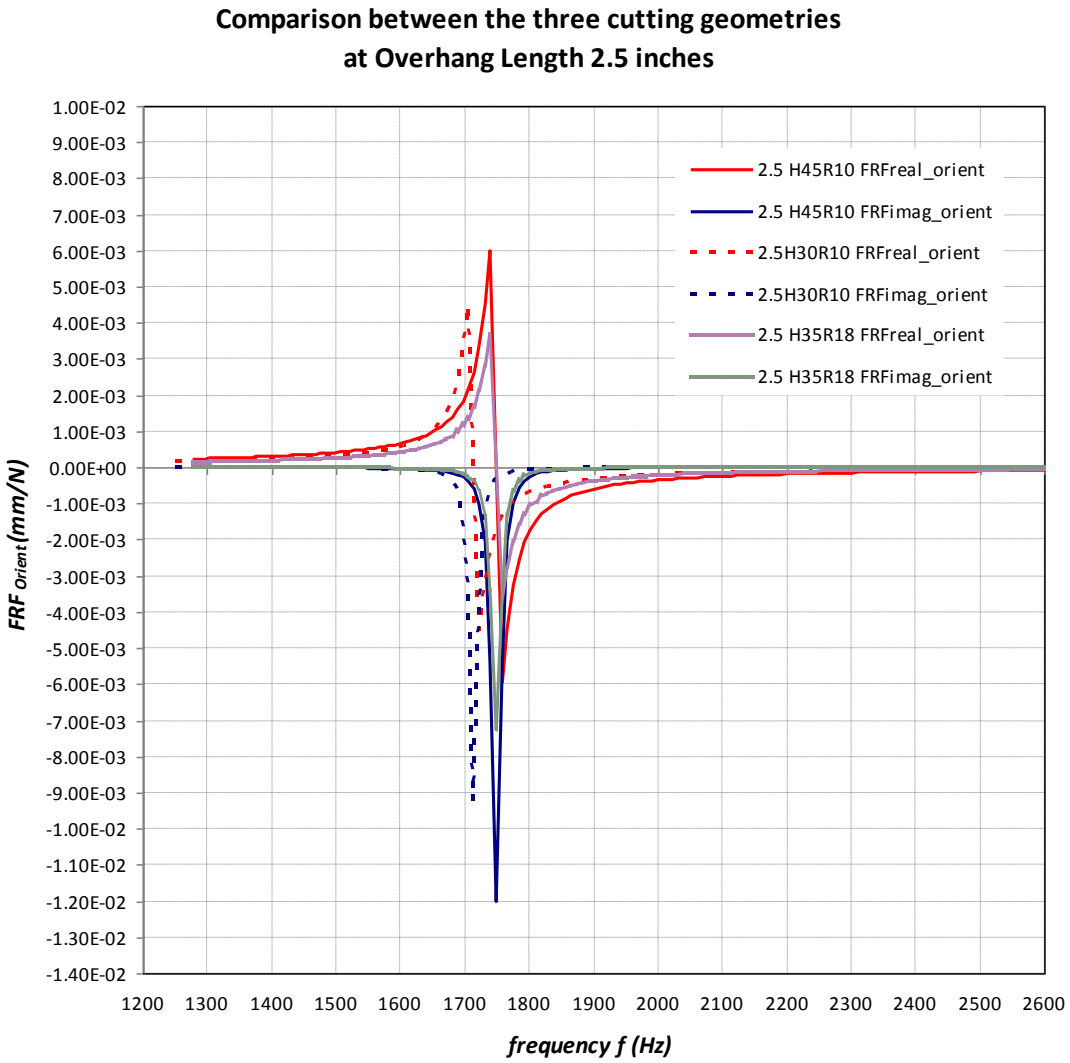

Figure B-1. Comparison of real and imaginary parts of three geometries at 2.5-inch overhang length.

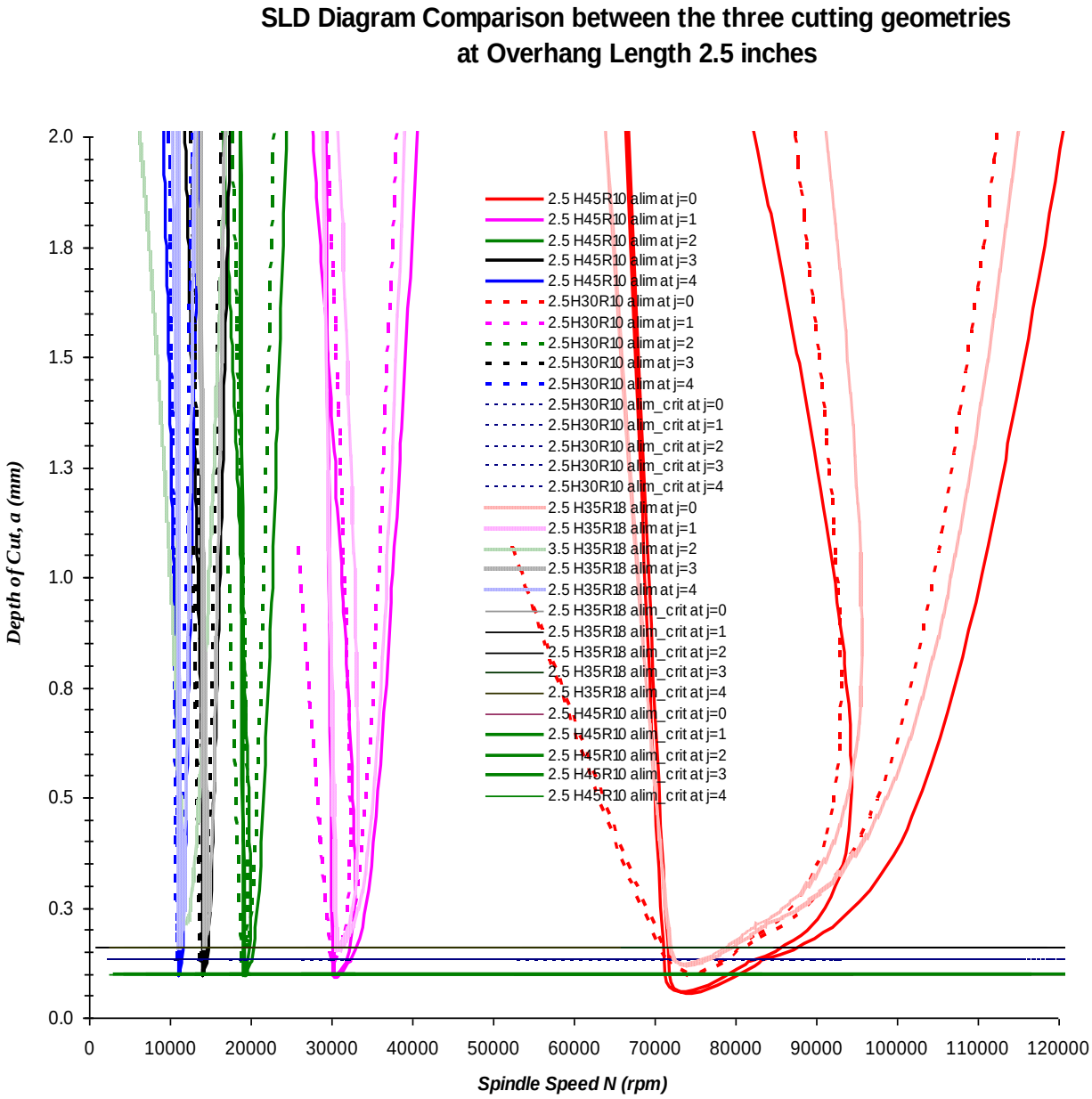

Figure B-2. Comparison of SLDs of three geometries at 2.5-inch overhang length.

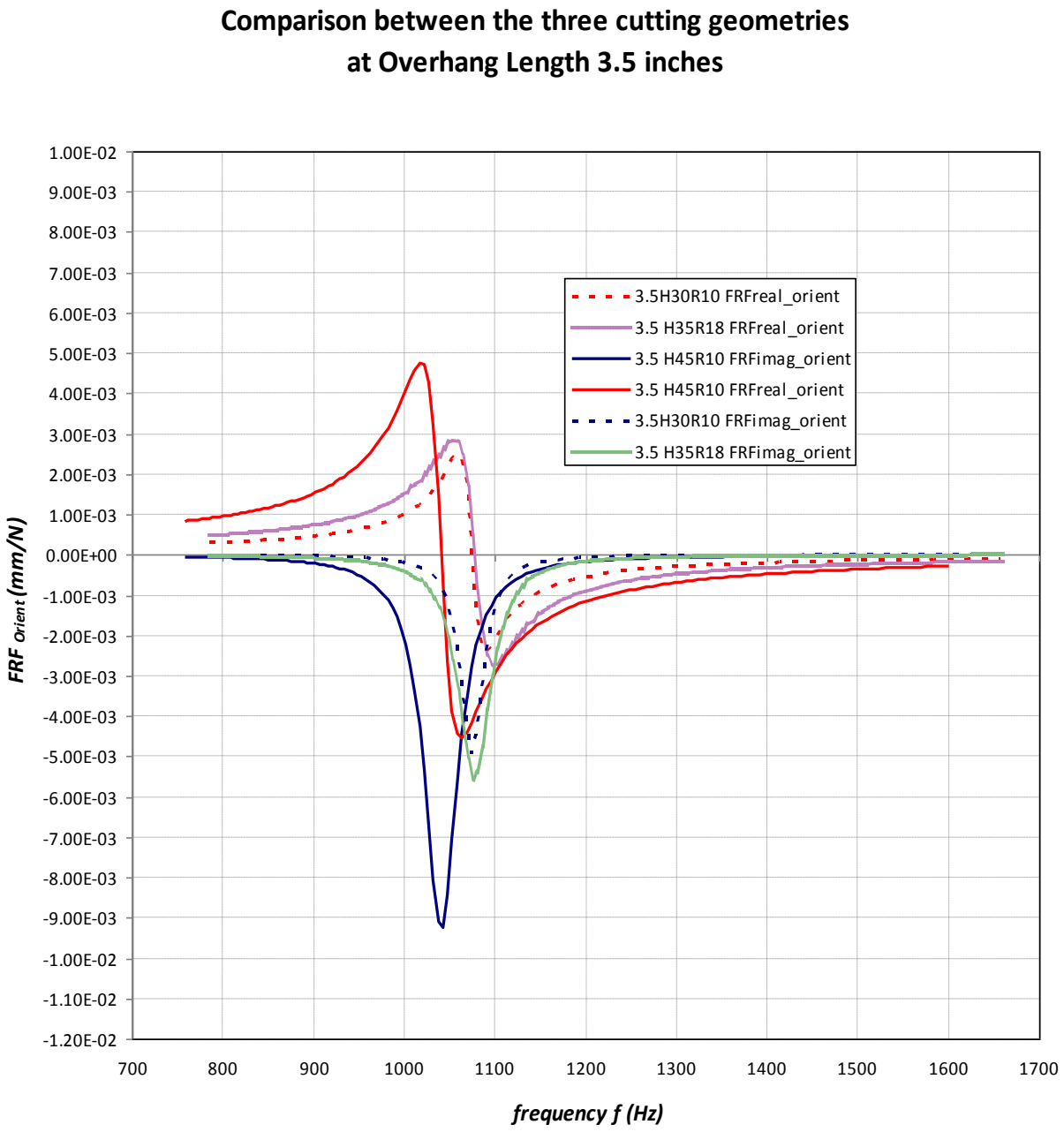

Figure B-3. Comparison of real and imaginary parts of three geometries at 3.5-inch overhang length.

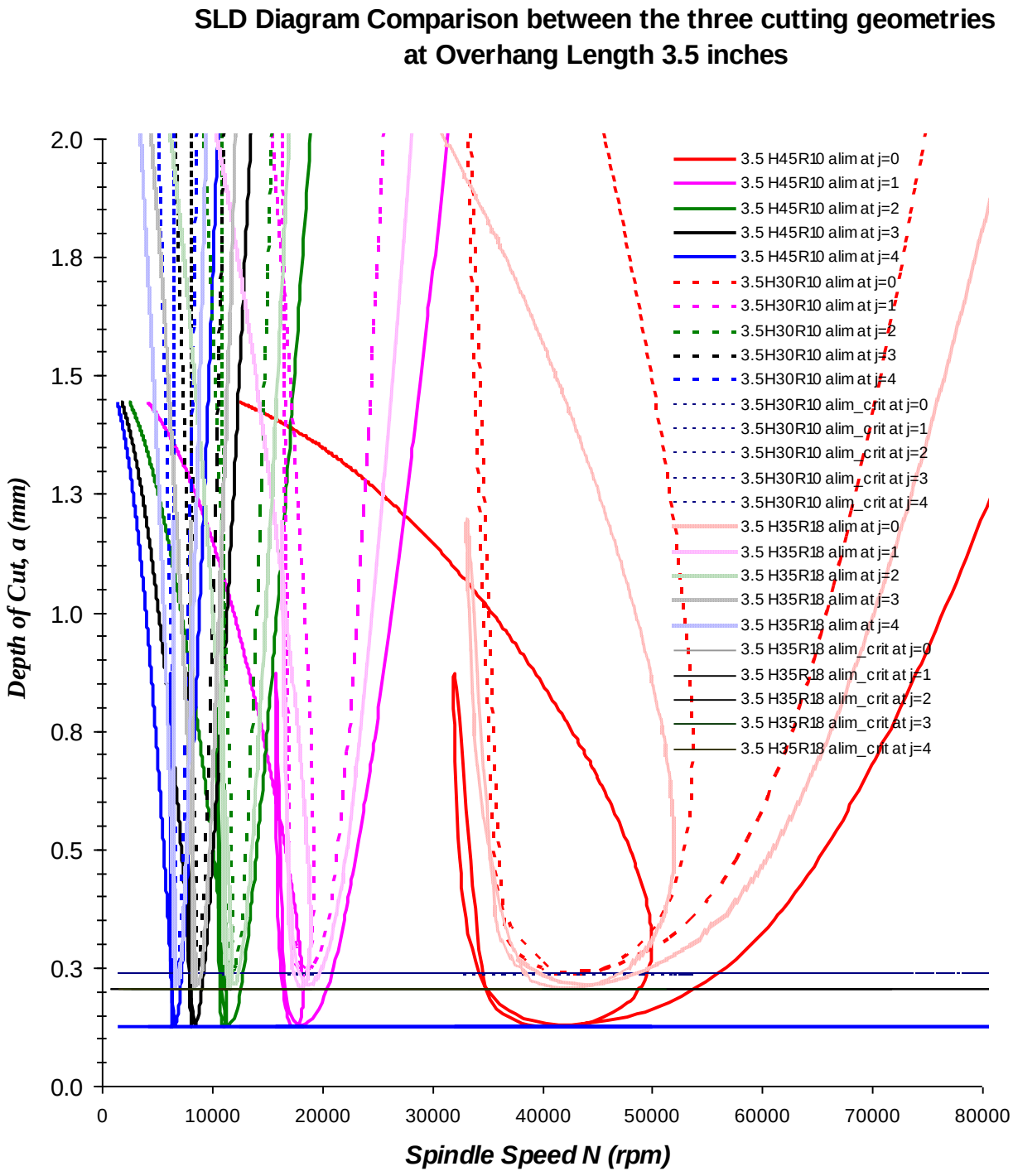

Figure B-4. Comparison of SLDs of three geometries at 3.5-inch overhang length.

APPENDIX C

BERNOULLI-EULER BEAM THEORY
(Craig and Kurdila, 2006)

The Bernoulli-Euler assumptions of elementary beam theory are as follows:

- The *x*-*y* plane is a principal plane of the beam and remains a plane as the beam deforms in the *y*-direction.
- An axis of the beam, which undergoes no extension or contraction, is called the *neutral axis* and is labeled the *x* axis. The original *xz* plane is called the *neutral plane*.
- Cross sections, which are perpendicular to the neutral axis in the undeformed beam, remain in the plane and perpendicular to the deformed neutral axis; that is, transverse shear deformation is neglected.
- The material is linearly elastic, with modulus of elasticity $E(x)$; that is, the beam is homogeneous at any cross section (generally, E = constant throughout the beam).
- Stresses σ_y and σ_z are negligible compared to σ_x.

To investigate the modal analysis of the carbide barstock or SL models and offer a general closed-form solution, an analytical model was introduced using the transverse vibration of Bernoulli-Euler beams. Transverse vibration of Bernoulli-Euler beams is governed by the following partial differential equation of motion:

$$\frac{d^2}{dx^2}\left(EI\frac{d^2}{dx^2}v(x,t)\right)+\rho A\frac{d^2}{dt^2}v(x,t)=0 \tag{C-1}$$

$$v(x,t)=V(x)\cos(\omega t-\theta) \tag{C-2}$$

where $v(x,t)$ is the transverse displacement, EI is the vertical bending stiffness, ρ is the mass density, and A is the cross-sectional area of the beam.

Assuming harmonic motion equation (C-2) and substituting it into equation (C-1) leads to

$$\frac{d^4}{dx^4}V(x) - \lambda^4 V(x) = 0 \tag{C-3}$$

where ω is the natural rotational frequency, θ is the phase angle, and λ can be written as

$$\lambda^4 = \omega^2 \frac{\rho A}{EI} \tag{C-4}$$

Since closed-form solutions are not available for the fourth-order ordinary differential equation given in equation (C-3) with variable coefficients, constant coefficients were considered for analysis of the beam. Therefore, the general solution may be written in the form of

$$V(x) = C_1 \sinh(\lambda x) + C_2 \cosh(\lambda x) + C_3 \sin(\lambda x) + C_4 \cos(\lambda x) \tag{C-5}$$

where C_1–C_4 are amplitude constant coefficients, and λ is the eigenvalue, both of which can be found using appropriate boundary conditions.

To arrive at a result, a solution of the form $V = e^{ax}$ is assumed, which will satisfy the differential equation when

$$a = \pm\lambda \qquad \text{and} \qquad a = \pm i\lambda$$

because

$$e^{\pm\lambda x} = \cosh\lambda x \pm \sinh\lambda x$$
$$e^{\pm i\lambda x} = \cosh\lambda x \pm i\sinh\lambda x$$

The solution to equation (C-5) is readily established, and the natural frequencies of vibration from equation (C-4) are found to be

$$f_r = \frac{(\lambda_r L)^2}{2\pi L^2}\sqrt{\frac{\mathrm{EI}}{\rho A}} \tag{C-6}$$

where the natural frequency is $\omega_r = 2\pi f_r$, r is the mode shape 1,2,3…, L is the length of the uniform bar, and the eigenvalue λ_r depends on the boundary conditions of the problem, as shown in Table C-1, where the numerical values of $(\lambda_r L)^2$ are listed for typical end conditions.

TABLE C-1

NUMERICAL VALUES OF $(\lambda_r L)^2$ FOR TYPICAL BOUNDARY CONDITIONS
(Thomson, 1993)

Beam Configuration	$(\lambda_1 L)^2$	$(\lambda_2 L)^2$	$(\lambda_3 L)^2$
Simply-Supported	9.87	39.50	88.90
Cantilever	3.52	22.00	61.70
Free-Free	22.40	61.70	121.00
Clamped-Clamped	22.40	61.70	121.00
Clamped-Hinged	15.40	50.00	104.00
Hinged-Free	0.00	15.40	50.00

APPENDIX D

DATA COLLECTION PROCESS

Here below are the data collection and modal analysis process for tests performed.

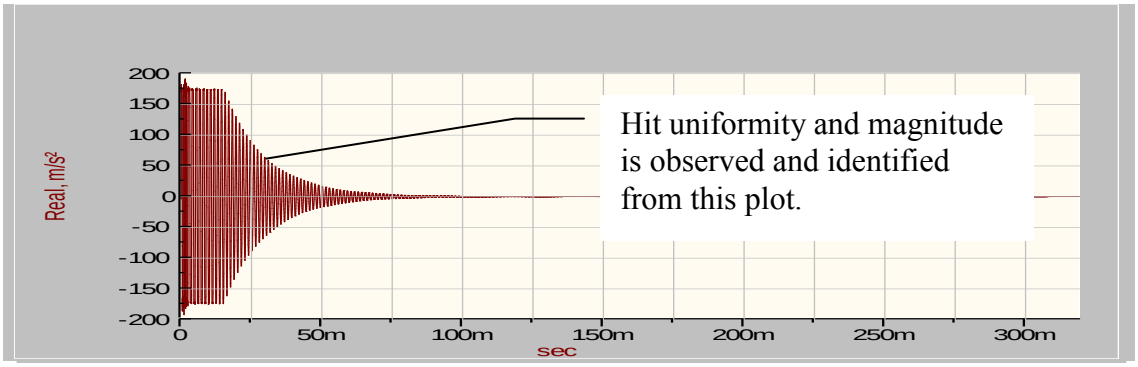

Figure D-1. Good quality of hit to accept data.

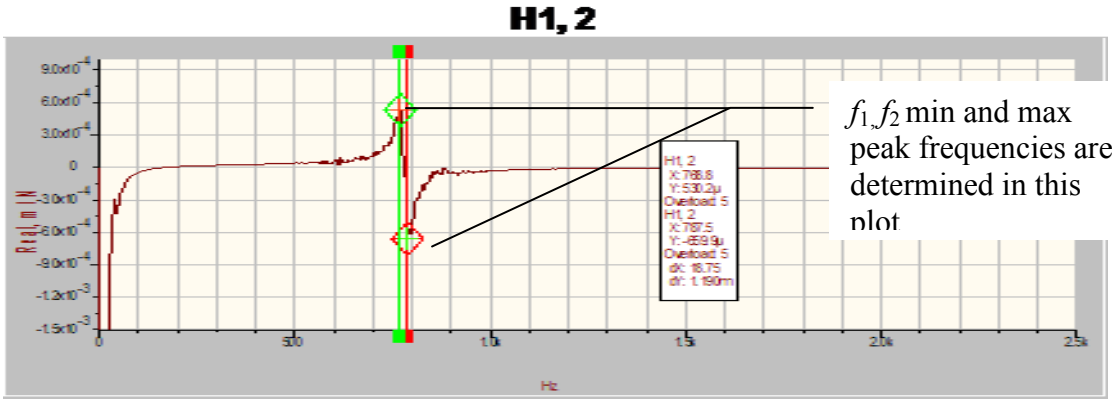

Figure D-2. Real part of FRF reading of peak frequencies.

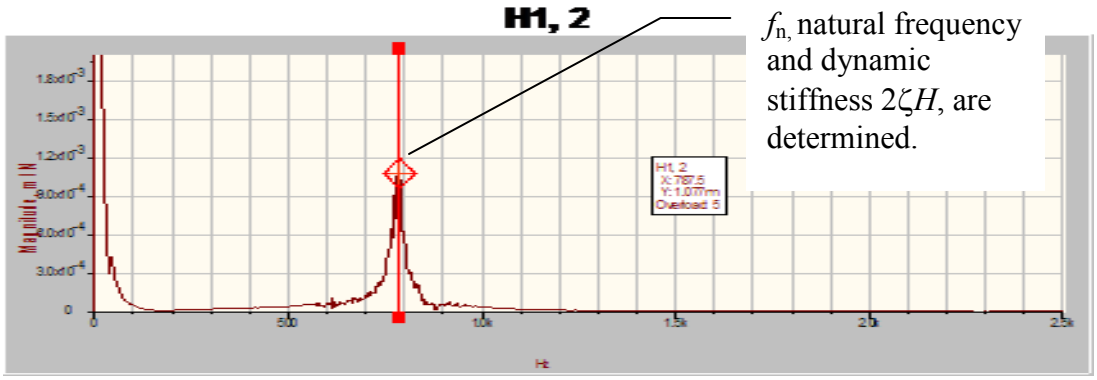

Figure D-3. Magnitude of FRF reading of peak frequencies.

Dynamic characteristics such as: damping ratio (ζ) and stiffness (k) are given by

$$\zeta = \frac{(f_2 - f_1)}{2f_n} \tag{D-1}$$

where ζ is the damping coefficient, f_1, f_2 and f_n are peak frequencies (Hz).

$$k = \frac{1}{2\zeta \mathrm{H}} \tag{D-2}$$

Where k is stiffness (N/m), ζ is the damping coefficient, and H the magnitude (m/N).

APPENDIX E

CERTIFICATES OF CALIBRATION

dp Data Physics corporation

Certificate of Calibration
for System No. 21158 SignalCalc Quattro – 2C
Date: June 3rd, 2010

Customer:

Wichita State University – Industrial and Mfg Eng
1845 Fairmont
Campus Box 35 Rm 120 Engineering
Wichita KS 67230
United States

Data Physics Corporation certifies that **System No. 21158** of the following hardware components:

Model:	Serial No:
DP240D	D47-064
DP240A	A65-064

Has been calibrated complying with MIL-STD-45662A/ANSI/NCSL Z 540-1-1994. The calibration instrument was a Hewlett Packard digital multimeter model 34401A, Serial No. US36062207 with Testwave LLC calibration certificate No. 09N4198.

The recommended calibration interval is 6 months. Based on this interval, the calibration due date is December 3rd, 2010.

Calibrated by:

Certified by:

1741 Technology Drive • Suite 260 • San Jose, CA 95110
TEL: 408.437.0100 • FAX: 408.437.0509 • www.dataphysics.com

~Calibration Certificate~

Model No.: 086C03 Customer:

Serial No.: 10709

Description: Impulse Force Hammer PO No.:

Manufacturer: PCB Calibration Method: Impulse (at-303-1)

Data

Output Bias: **10.4** Temperature: 73 °F 23 °C Relative Humidity: 38 %

HAMMER SENSITIVITY:

Hammer Configuration: Tip		Plastic/Vinyl	Plastic/Vinyl	
Extender		None	Steel	
Hammer Sensitivity	mV/lb	9.35	9.85	
	(mV/N)	2.10	2.22	

Above data is valid for all supplied tips.

Condition of Unit:

As Found In tolerance, no adjustment necessary.

As Left: In tolerance.

Special Note: Has 2

Notes:

1. Calibration is N.I.S.T traceable through project No. 822/274086 and PTB Traceable thru Project 1060.
2. This certificate may not be reproduced, except in full, without written approval from PCB Piezotronics, Inc.
3. Calibration is performed in compliance with ISO 10012-1, ANSI/NCSL Z540-1-1994.
4. See Manufacturer's specification sheet for a detailed listing of performance specifications.
5. Measurement uncertainty (95% confidence level with a coverage factor of 2) is +/-3.8%.

Technician: Brian Kemp BK Date: 6/16/2009

PCB PIEZOTRONICS
3425 Walden Avenue
Depew, N.Y. 14043
TEL: 716-684-0001 FAX: 716-684-0987 www.pcb.com

~ Calibration Certificate ~

Per ISO 16063-21

Model Number: 352B10

Serial Number: 113724

Description: ICP® Accelerometer Method: Back-to-Back Comparison (AT401-3)

Manufacturer: PCB

Calibration Data

Sensitivity @ 100.0 Hz	9.78	mV/g	Output Bias	9.9	VDC
	(0.997	mV/m/s²)	Transverse Sensitivity	2.3	%
Discharge Time Constant	0.3	seconds	Resonant Frequency	76.7	kHz

Sensitivity Plot

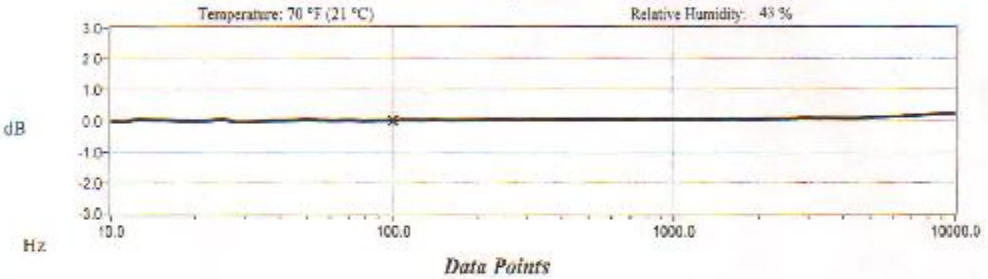

Data Points

Frequency (Hz)	Dev. (%)	Frequency (Hz)	Dev. (%)	Frequency (Hz)	Dev. (%)
10.0	-0.3	300.0	0.2	7000.0	1.7
15.0	0.0	500.0	0.3	10000.0	2.4
30.0	-0.4	1000.0	0.4		
50.0	0.2	3000.0	0.9		
REF. FREQ.	0.0	5000.0	1.0		

Condition of Unit

As Found: n/a

As Left: New Unit, In Tolerance

Notes

1. Calibration is NIST Traceable thru Project 822/277342 and PTB Traceable thru Project 1254.
2. This certificate shall not be reproduced, except in full, without written approval from PCB Piezotronics, Inc.
3. Calibration is performed in compliance with ISO 9001, ISO 10012-1, ANSI/NCSL Z540-1-1994 and ISO 17025.
4. See Manufacturer's Specification Sheet for a detailed listing of performance specifications.
5. Measurement uncertainty (95% confidence level with coverage factor of 2) for frequency ranges tested during calibration are as follows: 5-9 Hz; +/- 2.0%, 10-99 Hz; +/- 1.5%, 100-1999 Hz; +/- 1.0%, 2-10 kHz; +/- 2.5%.

Technician: Tammy Haskins Date: 05/04/10

ACCREDITED
CALIBRATION CERT #1982.01

PCB PIEZOTRONICS
VIBRATION DIVISION
Headquarters: 3425 Walden Avenue, Depew, NY 14043
Calibration Performed at: 10869 Highway 903, Halifax, NC 27839
TEL: 888-684-0013 · FAX: 716-685-3886 · www.pcb.com

APPENDIX F

MECHANICAL PROPERTIES FOR WATERSHED™ 11120 RESIN

WaterShed™ 11120

Durable, strong, semi-transparent, water-resistant resin for stereolithography
For Solid State (355 nm) Laser Systems

Description

DSM Somos® 11120 is a low viscosity liquid photopolymer that produces strong, tough, water-resistant parts. Parts created with Somos® 11120 have a light green tinge, similar in color to plate glass.

Application

Somos® 11120 offers many properties that mimic traditional engineering plastics including ABS and PBT. This makes the material ideal for many applications in the automotive, medical and consumer electronics markets and include:

- Water flow analysis
- RTV patterns
- Durable concept models
- Wind tunnel testing
- Quickcast patterns

Physical Properties – Liquid

Appearance	Optically clear
Viscosity	~260 cps at 30°C
Density	~1.12 g/cm³ at 25°C

Optical Properties at 355 nm

E_c	~11.5 mJ/cm²
D_p	0.16 mm (~.0065 inch)
E_0	54 mJ/cm²

DSM Somos
2 Penn's Way, Suite 401
New Castle, DE 19720, USA
Tel: +1 302.326.8100
Fax: +1 302.326.8121

DSM Desotech bv
3150 AB Hoek van Holland
The Netherlands
Tel: +31 1743.15391
Fax: +31 1743.15530

www.dsmsomos.com

Email:
Americas@dsmsomos.info
Europe@dsmsomos.info
Asia@dsmsomos.info

Mechanical Properties (Metric)

ASTM Method	Description	WaterShed™ 11120	ABS* (transparent)	Polybutylene Terephthalate*
D638M	Tensile Strength	47.1 - 53.6 MPa	45.7 MPa	55 MPa
	Elongation at Break	11 - 20 %	41.6 %	20 %
	Elongation at Yield	3.3 - 3.5 %	N/A	3.5 - 9 %
	Modulus of Elasticity	2,650 - 2880 MPa	2,000 MPa	2,700 MPa
D790M	Flexural Strength	63.1 - 74.16 MPa	73.5 MPa	80 MPa
	Flexural Modulus	2,040 - 2370 MPa	2,300 MPa	2,500 MPa
D256A	Izod Impact-Notched	0.2 - 0.3 J/cm	1.6 J/cm	1.2 J/cm
D542	Index of Refraction	1.512 - 1.515	1.52	N/A
D2240	Hardness (Shore D)	N/A	N/A	98 - 120 (Rockwell R)
D1004	Graves Tear	150,288 N/m	N/A	N/A
D570-98	Water Absorption	0.35 %	0.20 – 0.45 %	0.16 %

* http://www.matweb.com N/A: Not Available

Thermal & Electrical Properties (Metric)

ASTM Method	Description	WaterShed™ 11120	ABS* (transparent)	Polybutylene Terephthalate*
E831-00	C.T.E. -40°C – 0°C	66 - 67 µm/m-°C	60 – 130 µm/m-°C (no temp range given)	50 - 145 µm/m-°C (no temp range given)
	C.T.E. 0°C – 50°C	90 - 96 µm/m-°C		
	C.T.E. 50°C – 100°C	170 - 189 µm/m-°C		
	C.T.E. 100°C – 150°C	185 - 189 µm/m-°C		
D150-98	Dielectric Constant 60Hz	3.9 - 4.1	3.7	
	Dielectric Constant 1KHz	3.7 - 3.9		2.9 - 4.0 (no frequency specified)
	Dielectric Constant 1MHz	3.4 - 3.5	3.7	
D149-97a	Dielectric Strength	15.4 - 16.3 kV/mm	13.8 – 19.7 kV/mm	14.7 - 30 kV/mm
E1545-00	Tg	39 - 46 °C		41 °C
D648-98c	HDT @ 0.46 MPa	45.9 - 54.5 °C	94 – 207 °C	150 °C
	HDT @ 1.81 MPa	49.0 -49.7 °C	86.4 – 194 °C	61.3 °C

* http://www.matweb.com N/A: Not Available

The ProtoFunctional™ Materials Company

DSM Somos® DSM

Mechanical Properties (Imperial)

ASTM Method	Description	WaterShed™ 11120	ABS* (transparent)	Polybutylene Terephthalate*
D638M	Tensile Strength	6831 - 7774 psi	6,628 psi	7977 psi
	Elongation at Break	11 - 20 %	41.6 %	20 %
	Elongation at Yield	3.3 - 3.5 %	N/A	3.5 - 9 %
	Modulus of Elasticity	384 - 418 kpsi	290,000 psi	391,602 psi
D790M	Flexural Strength	9,152 - 10,756 psi	10,660 psi	11,603 psi
	Flexural Modulus	296 - 344 kpsi	344,000 psi	362,594 psi
D256A	Izod Impact-Notched	0.4 - 0.6 ft lb/in	1.5 - 2.0 ft lb/in	0.56 ft lb/in
D542	Index of Refraction	1.513 - 1.515	1.52	N/A
D2240	Hardness (Shore D)	N/A	N/A	98 - 120 (Rockwell R)
D1004	Graves Tear	833 - 858 lbf/in	N/A	N/A
D570-98	Water Absorption	0.35 %	0.2 - 0.45 %	0.16 %

* http://www.matweb.com N/A: Not Available

Thermal & Electrical Properties (Imperial)

ASTM Method	Description	WaterShed™ 11120	ABS* (transparent)	Polybutylene Terephthalate*
E831-00	C.T.E. -40°F – 32°F	37 µin/in-°F	33 – 72 µin/in-°F (no temp range given)	28 - 81 µin/in-°F (no temp range given)
	C.T.E. 32°F – 122°F	50 - 53 µin/in-°F		
	C.T.E. 122°F – 212°F	94 - 105 µin/in-°F		
	C.T.E. 212°F – 302°F	103 - 105 µin/in-°F		
D150-98	Dielectric Constant 60Hz	3.9 - 4.1	3.7	
	Dielectric Constant 1KHz	3.7 - 3.9		2.9 - 4.0 (no frequency specified)
	Dielectric Constant 1MHz	3.4 - 3.5	3.7	
D149-97a	Dielectric Strength	390 - 413 V/mil	350 - 500 V/mil	373 -762 V/mil
E1545-00	Tg	102 - 109 °F		106 °F
D648-98c	HDT @ 0.46 MPa	115 - 130 °F	201 - 405 °F	302 °F
	HDT @ 1.81 MPa	120 °F	187 - 381 °F	142.3 °F

* http://www.matweb.com N/A: Not Available

The ProtoFunctional® Materials Company

DSM Somos® DSM